Polarized Target Experiments
Using the
CEBAF Large Acceptance Spectrometer

V. Burkert, B. Mecking
CEBAF
Newport News, Virginia

D. Day, J. McCarthy, R. Minehart
University of Virginia
Charlottesville, Virginia

Abstract

The general features of the physics program that can be carried out using solid–state polarized hydrogen and deuterium targets and the CEBAF Large Acceptance Spectrometer are outlined. The practical aspects of these experiments are discussed. Two specific examples are worked out in some detail: deuteron electro–disintegration and the electro–production of pions in the region of the Roper resonance.

I. Introduction

The study of nuclear and hadronic structure at CEBAF will be considerably enhanced through the use of a polarized electron beam and polarized targets. In inclusive scattering, new structure functions can be measured which are not accessible without the use of the spin degrees of freedom.[1] An example of particular interest is the structure function that involves the interference of transverse and longitudinal amplitudes (W^{TL} in the notation of ref. 1). This structure function provides clean information on longitudinal and transverse amplitudes which are often difficult to disentangle by Rosenbluth separation in unpolarized experiments. It also provides new information such as the relative sign of the amplitudes. The structure function W^{TL} is selected by orienting the target spin perpendicular to the momentum transfer direction.

Additional power to separate different amplitudes and multipoles can be obtained by detecting one or more of the hadronic reaction products in the final state.[2] Such measurements will be necessary to extract multipole amplitudes for individual nucleon resonances in the presence of non-resonant background and possible interference from other resonances. An interesting measurement has been proposed to study the properties of the Roper resonance in single π production from a polarized proton target. At CEBAF, such experiments will be of high interest, and it is in this area that the full power of the CEBAF facility will be utilized. Due to its ability to accommodate polarized targets and beams while providing large acceptance for detection of reaction products, the CEBAF Large Acceptance Spectrometer (CLAS) will clearly be a valuable tool in this area of research.

For polarized target experiments, the luminosity limitation of the CLAS is not a disadvantage since, with present technology, only moderate luminosity can be achieved both for polarized ^{3}He targets[3,4] and for solid-state targets[5,6]. Solid-state polarized hydrogen (and deuterium) targets are limited in the amount of electron beam intensity that they can withstand without significant radiation damage. The maximum luminosity is limited to about $\sim 5 \times 10^{34} \text{cm}^{-2}\text{sec}^{-1}$ for radiation-resistant ammonia targets (the luminosity is given in terms of the total number of nucleons in the target including the nitrogen background material). This limit is actually well matched to the expected luminosity limitation of the CLAS. The large acceptance of CLAS is always important in achieving reasonable count rates with these targets, even in inclusive experiments.

An additional natural advantage of the CLAS for solid-state polarized target work is its tolerance of the large magnetic holding field associated with hydrogen and deuterium solid-state polarized targets. The 5 Tesla field deflects both the electron beam and the reaction products (such as the scattered electron) significantly. This complicates the use of standard "small acceptance" focussing spectrometers of high optical quality due to the distortion of their optical properties and their acceptance function. To use a focussing spectrometer, one would have to displace the target or the spectrometer in such a way that the desired particles are transmitted to the focal plane. CLAS can tolerate these high fields in the target region; the particle trajectories can be reconstructed to retrieve the kinematic quantities of interest. It is important to note that the field-free region at the target position is a valuable feature of the CLAS design. This will allow the target spin to be oriented along an arbitrary axis, which is necessary in most experiments.

In the course of the development of the CLAS capabilities, the use of solid–state polarized targets is viewed as a second generation venture. The operation of a polarized target is also complicated. Both devices should only be combined after they have been tested individually.

To illustrate the use of the CLAS with polarized targets and a polarized electron beam, an experiment to measure the scattering of polarized electrons on polarized deuterium will be described in the following. The physics motivation is the measurement of the neutron electric form factor which is currently of high interest and a test of the deuteron wave function. For the measurement of the neutron electric form factor, electron–neutron scattering events are selected via coincident neutron detection along the momentum transfer direction. While this part of the experiment does not need the detection of uncorrelated multi–particle hadronic final states, it already illustrates the power of the CLAS for polarized target experiments even for simple two–body final states. Of course, the advantage of using the CLAS will be even greater for more complex final states. As a second example, we will discuss a measurement in the nucleon resonance region using a polarized proton target.

The polarized solid–state target that is presently under development at the University of Virginia will be a general purpose device usable in all three of CEBAF's experimental halls. Some aspects of this program will be covered by first–generation experiments at CEBAF using the standard spectrometers.

In the following section, we will demonstrate that unique advantages will be offered by the CLAS detector. Some general aspects related to the use of polarized solid state targets in electron beams are discussed in section II, and the specific problems of using polarized solid state targets with CLAS will be discussed in section III. The measurement of the asymmetry in the scattering of polarized electrons on a polarized deuterium target will be adressed in section IV. The target polarization asymmetry in the study of single pion electroproduction are discussed in section V. Applications in the study of the Roper resonance will be discussed in section VI.

II. Technical Aspects of Solid–State Polarized Targets

II.1 Polarized Target Materials.

For a long time, one of the main obstacles for using solid state targets in intense ionizing particle beams has been the low resistance of the standard target materials, like butanol, to radiation damage. With the emergence of NH_3 and ND_3 as polarized target materials for protons and deuterons, these problems have largely been solved.

The basic difference between these new materials and the ones used previously is that the free electrons which are necessary for the dynamic polarization mechanism were generally added in the form of paramagnetic chemicals (e.g. 2–5% of porphyrexide in the case of butanol) whereas in NH_3 and ND_3 the free electrons are produced by exposing the target sample to an intense beam of ionizing particles, e.g. electrons. In order to

obtain a sufficiently high density of free electrons, an irradiation dose of approximately 10^{17} electrons/cm^2 at a temperature of 80 K is required.

The qualitative performance of NH$_3$ and ND$_3$ under additional irradiation in a 1.5 GeV electron beam at the regular working temperature of the target cryostat (< 1 K) is shown in Figure 1 - Figure 3. For pre–irradiated NH$_3$, the polarization, after an initial drop, remains constant at a level of $\sim$ 70% of the initial polarization. The initial polarization can be easily recovered by heating the target sample to 75 Kelvin for about 15 minutes. For pre–irradiated ND$_3$, the polarization first rises to a maximum value (at $\sim 0.4 \times 10^{15}$ electrons/cm^2) which is appreciably larger than the initial polarization value, and then drops asymptotically to a constant value of $\sim$ 75% of the maximum polarization. The initial conditions are reproduced by heating up the target sample to a temperature of 75 K.

It should be noted that these measurements have been performed at 1 K and with a magnetic field of 2.5 Tesla. At lower temperatures and higher magnetic fields the absolute polarization is considerably higher; the qualitative behavior, however, does not change.

The pre–irradiation may be performed within approximately one hour in an electron beam of 50 μA. To achieve a uniform irradiation and avoid inhomogeneous polarization of the target sample, it will be necessary to scan the electron beam across the full target area during pre–irradiation in the high intensity electron beam and also during the actual experiment.

II.2 Cryogenic Requirements.

The maximum achievable polarization depends strongly upon the working temperature of the target cryostat and the strength of the magnetic field at the target sample. Figure 4 shows the proton polarization measured at working temperatures of 1000mK, 500mK, and 250mK. These temperatures can be achieved using different types of cryostates with different coolants. With ^4He as coolant, temperatures of typically 1000mK are achieved, the precise value being dependent upon the power of the pumping units used to pump the ^4He gas. With ^3He temperatures of typically 500mK are achieved. A drawback of using pure ^3He as coolant is the much lower heat transport capability compared to superfluid ^4He. Using a $^3He/^4He$ mixture ("dilution cryostates"), cryostate operation temperatures of 160mK to 400mK can be achieved dependent on the heat loading due to the incident beam. Recent studies of the deuteron polarization in ND$_3$ are summarized in Figure 5.

Since the deuteron is a spin 1 particle, the magnetic quantum number m_z may adopt the values $m_z = 0, \pm 1$. Hence, in addition to the usual vector polarization

$$P_z = \frac{N_+ - N_-}{N_+ + N_o + N_-},$$

the deuterons may also be tensor polarized with the polarization P_{zz}:

$$P_{zz} = \frac{N_+ + N_- - 2N_o}{N_+ + N_o + N_-}$$

N_+, N_-, N_o being the population of the $m_x = +1$, 0 states, respectively.

At a temperature of T = 200 mK and a magnetic field B = 3.5 Tesla, a vector polarization P_x=0.5 has been achieved with ND_3. At this vector polarization, an appreciable tensor polarization is obtained as a byproduct of the dynamic polarization mechanism. In the thermal equilibrium, assuming equal spin temperatures, the tensor polarization P_{xx} is related to the vector polarization P_x by:

$$P_{xx} = 2 - \sqrt{4 - 3P_x^2}$$

To give an example, a vector polarization of P_x=0.6 results in a tensor polarization P_{xx}=0.3 which is sufficient for experiments that are sensitive to P_{xx}.

Using standard dynamic polarization techniques, a higher tensor polarization can be obtained only at low temperatures (T < 300 mK) where the cooling power of the target cryostat is low. The limited cooling power provides the ultimate limitation for the electron beam current which the polarized target can tolerate. In Figure 6 the measured cooling power of two types of cryostats for polarized target experiments are displayed versus the operating temperature. The "Bonn cryostat" could be operated at a cooling power of 20 mW at 270 mK with the 1.6 cm long ND_3 target exposed to an average electron current of I=0.3 to 0.4 nA. With a magnetic field of B=3.5 Tesla, an average vector polarization P_x=0.47 and a tensor polarization P_{xx}=0.17 have been achieved. These polarization values could be maintained during a running period of about one week.

The cryostat of the EMC polarized target can handled an approximately 1 meter long NH_3 target with a cross section of 5 x 6 cm^2, whereas the Bonn polarized target has a much smaller volume of 2.5 x 2.5 x 1.6 cm^3. With some modifications in the pumping system and with changes in the size and arrangement of the cooling pipes for the $^3He/^4He$ mixture, it seems feasible to increase the cooling power by a factor of 10 - 20 for the type of dilution cryostat used at Bonn. An average electron current of ~ 4 to 8 nA at a temperature of T ~ 270 mK therefore seems a realistic design goal for a cryostat to be used at CEBAF.

II.3 Magnetic Field Considerations.

For achieving a high proton or deuteron polarization, a magnetic field of greater than 2.5 Tesla with a good field uniformity ($\Delta B/B < 10^{-4}$) over the full target volume is required. The magnetic field dependence of the maximum deuteron polarization at T ~ 200 mK is shown in Figure 7 for ND_3 and LiD. Although no data exist for ND_3 at field values above 3.5 Tesla, the comparison with the LiD data suggests that a deuteron vector polarization of P_x=0.6 and a tensor polarization P_{xx} > 0.3 can be achieved at 5 Tesla. The requirement of a large magnetic field over the target volume poses certain limitations on the accessible kinematical regions for a number of experiments.

(1) The experimentally accessible solid angle is limited to the coil-free space. In addition, there will be a further solid angle obstruction due to the magnet cryostat and the support structure.

(2) Dependent on the integrated field strength, there is a low momentum cut off for the detection of charged particles. For this reason it is highly desirable to make the magnetic field volume, and the integrated field length as small as possible.

The coil size basically depends upon the target volume and the required field uniformity. For experiments at CEBAF a target volume of 25 x 25 x 25 mm^3 would be appropriate. The advantage of a small target size is that the corresponding coil system can be realized with a smaller dead zone for the outgoing particles.

A coil geometry has been developed that provides the required field conditions at a central field of 4 Tesla for a target volume of 30 x 30 x 30 mm^3. Figure 8 shows the design of a polarized target magnet with a coil optimized for minimum obstruction of solid angle, and maximum field homogeneity. Note that in this design the forward region is completely open in a cone with an opening angle of 102°. Sideways the angular range from 77.5° to 102.5° is accessible. With a more optimized design of the magnet cryostat the large angle acceptance could possibly be extended. Using this coil geometry the field distribution was calculated, and the effects of the polarized target field on the performance of the CLAS detector were studied.

III. Performance of the CLAS Detector with Polarized Target Field.

The axial field component B_z is shown in Figure 9 as a function of r and z. For a central magnetic field of 5 Tesla on obtains $\int Bdl = 1.0$Tm. Deflection of charged particles in the target field might therefore seriously affect acceptance of charged particles in CLAS. Clearly, the largest deflection will occur for particles emitted at 90° with respect to the symmetry axis of the target field. Figure 10 displays charged particle trajectories with momenta between 150MeV/c and 2000MeV/c. Low momentum particles are strongly deflected in the polarized target field. The magnetic field causes effectively a low momentum cut-off at $\approx$ 150MeV/c. Besides this cut-off, the CLAS acceptance for single particles is only slightly affected if one ignores the fact that the ϕ acceptance is shifted by an angle $\Delta\phi(p)$. It is worth mentioning that the particle trajectories after leaving the polarized target field region still appear to be pointing back to the emission point at the target. Momentum resolution for reconstructed trajectories is –to first order– not affected by the presence of the magnetic field, since most of the $\int Bdl$ is concentrated inside the region where the CLAS tracking chambers are located. Similarly, the resolution in the polar and azimuthal scattering angle is not affected by the presence of the target field, assuming the target field distribution is known with sufficient precision.

III.1 Beam Handling in Polarized Target Operation.

In most applications of polarized targets pertaining to the study of nucleon resonance excitation the polarization vector is aligned parallel to the direction of the incident electron beam. In this configuration the primary beam is unaffected, except for the (minor) focussing properties of the target field. In some experiments, however, the polarization vector and hence the orientation of the magnetic field will have an angle $\neq$ 0 relative to the beam axis. As a consequence, the incident electron beam will also be deflected in the magnetic field of the polarized target. For a 2GeV incident electron beam the deflection

can be as large as $13°$ if the target field is oriented perpendicular to the incident beam direction. To make sure that the beam is directed towards the beam dump, some beam manipulations will be necessary in this case.

We envisage adoption of the following scheme for operating a polarized target in CLAS:

(i) Compensation of beam deflection.

Because of the azimuthal symmetry of CLAS, all possible polarization configurations can be achieved by rotating the magnetic field direction horizontally by an angle ψ. The incident beam is then deflected vertically by an angle $\alpha_v(\psi)$. This deflection is compensated by bringing in the beam at an angle $-\alpha_v$. The incident beam has therefore an angle $\alpha_v/2$ at the center of the target. After fully traversing the polarized target field, the beam is directed towards the beam dump. Bremsstrahlung produced in the target is emitted from the target at an angle $\alpha_v/2$. To protect the CLAS detectors against the intense flux of bremsstrahlung a wedged shaped lead block will be positioned in the corresponding CLAS sector. For most of the experiments shielding of the angular region below $6°$ will be sufficient, which will not affect the acceptance of the CLAS detector.

(ii) Beam rastering.

The polarizability of the protons and deuterons in NH_3 and ND_3 strongly depends upon their exposure to ionizing particle beams. In fact, both materials must be preirradiated with about 10^{17} particles per cm^2 to reach their optimum performance. In case of a physics experiment, the polarization degree can change (increase or decrease) depending on the history of the target sample. To avoid local depolarization or polarization buildup, due to non uniform exposure of the target sample to the beam, the incident beam will be scanned across the target front face. In order to avoid local temperature rise within the target sample, high speed beam rastering is necessary. This can be achieved by incorporating four small dipole magnets upsteams in the beam line, made of laminated magnetic steel.

III.2 Background and Luminosity Issues for Polarized Target Operation.

Since a polarized solid state target has a strong magnetic field associated with it, the trajectories of charged background particles coming from the target region will be strongly influenced by the field orientation chosen for a specific experiment. The use of a polarized target has been studied for two cases [18]:

(i) Target is polarized along the beam direction.
(ii) The target is polarized at $20°$ with respect to the beam direction.

The target sample used in the simulation is in the shape of a cylinder of 1.5cm length and 1cm radius.

(i) Target polarized along the beam direction.

Such a configuration will e.g. be used in the study of baryon resonance excitation in single pion electroproduction. In this case, the longitudinal magnetic field of the target acts like a focussing lens, and keeps practically all low energy charged particles emerging from the target within a narrow cone surrounding the beam axis, even those that were

emitted at large angles. Figure 11 shows the particle trajectories through the magnet. This shielding is at least as effective as the shielding using the standard miniature torus. The wire chambers appear to be nearly unaffected by charged background. Therefore, we can expect the CLAS detector to safely operate at luminosities of 10^{34} cm^{-2}sec^{-1} (and possibly beyond) in conjunction with a polarized target having the polarization axis aligned along the beam axis.

(ii) Target polarized at 20° to the beam direction.

Such a configuration would, for example, be used for measuring the electric formfactor of the neutron. As the polarized target field now contributes to the deflection of electrons and positrons near the primary beam direction, the simulation had to include even the very forward-going particles with scattering angles smaller than 2°. Figure 12 displays trajectories in the CLAS for such a situation. We obviously encounter a more involved background situation than in the previous case. As the forward-going beam, after penetrating the target, contains electrons and positrons with a wide momentum spectrum, it is likely that additional shielding near the beam pipe will be necessary to protect the detectors against electrons which would otherwise be swept into the sensitive detector region. No optimization of the shielding geometry has been done. However, simple shielding of the beam pipe downstream of the target, in conjunction with additional shielding of the polarized target area appears to improve background situation decisively. Figure 13 shows the background situation for a luminosity of $3 \cdot 10^{33}$ cm^{-2}sec^{-1}. The specific target orientation chosen, together with the charge asymmetry of the background yield (mostly electrons) results in a non-uniform distribution of background hits in the six CLAS sectors. In fact, it appears that only one sector is affected by charged background hits in a significant way. Note that this particular sector would not be used in the G_E^n measurement, and the sensitive detector components could therefore be shut off. We expect that, under more optimized shielding conditions, luminosities of up to 10^{34}cm^{-2}sec^{-1} will be feasible. This would allow the operation of polarized solid state targets in CLAS, with luminosities near the limit of what these devices can presently tolerate.

Note that the simulations were done with the CLAS configuration as outlined in the Preliminary Conceptual Design Report [17].

III.3 Mechanical Aspects of Polarized Target Operation in CLAS.

The mechanical support structure has to serve two functions, it holds the target magnet in place, and it has to carry the magnetic forces resulting from the interference of the target field with the main torus field. It should also not obstruct any additional solid angle. The present design makes use of a rigid connection of the magnet cryostat with the torus cryostat in the rear. Figure 14 shows the layout of the target magnet, the target cryostat, and the support structure in the CLAS magnet as presently envisaged.

IV. Measurement of the Asymmetry in the Scattering of Polarized Electrons on a Polarized Deuterium Target

A measurement of the asymmetry in the scattering of polarized electrons on a polarized deuterium target allows one to extract the neutron electric form factor G_E^n and to perform various tests to check the validity of both experimental and theoretical techniques. One can also test the validity of the standard description of the deuteron wave function.

The knowledge of G_E^n is important for several reasons. First, it is a quantity that is fundamental for our understanding of the nucleon. Unfortunately, there is very little experimental information; the charge distribution of half of all matter surrounding us is essentially unmeasured. Secondly, G_E^n is essential for the interpretation of Coulomb and electric multipoles in nuclei. A good example is the dependence of the deuteron electric structure function $A(Q^2)$ on G_E^n at high Q^2.

Experimental information on the neutron electric form factor is very poor for all non-zero values of Q^2. In the absence of a free neutron target, one has to rely on scattering from few–nucleon systems. Unlike for the proton, the Rosenbluth separation of G_E^n from G_M^n is difficult even at low Q^2 because of the small size of G_E^n compared to G_M^n. At $Q^2 = 0$, the charge form factor G_E^n must be zero. At low Q^2, G_E^n would be non–zero only if the charge distribution within the neutron were non–uniform. The slope of G_E^n versus Q^2 at low Q^2 has been measured accurately[7]; it is positive, indicating that the neutron has a slightly positive core surrounded by a region of negative charge.

Figure 15 shows the measured electric neutron form factor as extracted from elastic electron–deuteron scattering data taken at DESY[8]. To extract $G_E^n(Q^2)$ from the data, it is necessary to assume a model for the deuteron structure. The data were analyzed with three different models: Hamada–Johnston, McGee, and Feshbach–Lomon. The best fit to the experimental data was obtained with the Feshbach–Lomon wave function and the parameterization

$$G_E^n(Q^2) = -\frac{\mu_n \cdot \tau}{1 + 5.6\tau} G_E^p(Q^2)$$

where $\tau = \frac{Q^2}{4M^2}$. However, it is obvious from the data that the value of $G_E^n(Q^2)$ is quite uncertain at all non–zero Q^2. In particular, the relation

$$G_E^n = -\tau G_M^n$$

is also consistent with the data. This relation holds if the Dirac form factor, F_{1n}, of the neutron is zero. In the Gari–Krumpelmann[9] and Korner–Kuroda[10] models, F_{1n} is very close to zero for all Q^2 due to cancellations. This parameterization is also the asymptotic QCD prediction. It is also supported by the data on the electric structure function of the deuteron $A(Q^2)$ at high Q^2. Furthermore, it is consistent with the measured slope at $Q^2 = 0$.

Two methods have been proposed to measure this fundamental quantity in a model independent way. One method to extract $G_E^n(Q^2)$ from the scattering of polarized electrons off unpolarized neutrons is to measure the neutron recoil polarization in a second scattering experiment[11]. An alternative method is to use quasi–elastic scattering of polarized electrons on vector polarized deuterium. In either case, the measured polarization asymmetry is proportional to the ratio G_E^n/G_M^n if the target neutrons are polarized perpendicular to the direction of the virtual photon. Measurement of the asymmetry thus allows one to extract G_E if G_M is known. In the following, we will discuss details of this method related to its application with CLAS.

Quasi–elastic scattering of electrons on deuterium with the neutron detected in the direction of the virtual photon is dominated by electron–neutron scattering. Therefore, we will consider the elastic scattering of a polarized electron by a polarized neutron. Figure 16 shows the relevant kinematic and spin vectors. Note that θ^* is the angle between the momentum transfer vector $\vec{q}$ and the nucleon spin, and $\phi^* = 0$ for the nucleon spin lying in the reaction plane. The helicity asymmetry is defined as:

$$A = \frac{\sigma_+(\theta,\theta^*,\phi^*) - \sigma_-(\theta,\theta^*,\phi^*)}{\sigma_+(\theta,\theta^*,\phi^*) + \sigma_-(\theta,\theta^*,\phi^*)}$$

where σ_+ (σ_-) corresponds to positive (negative) electron helicity.

For elastic scattering of a polarized electron from a free polarized neutron, the asymmetry is given by

$$A_{en} = \frac{2\tau\cos\theta^* v_T' + 2\sqrt{2\tau(1+\tau)}\cdot(G_E^n/G_M^n)\sin\theta^*\cos\phi^* v_{TL}'}{v_L(1+\tau)\cdot(G_E^n/G_M^n)^2 + 2\tau v_T}$$

where

$$v_L = \left(\frac{Q^2}{q^2}\right)^2$$

$$v_T = \frac{Q^2}{2q^2} + \tan^2\frac{\theta}{2}$$

$$v_T' = \tan\frac{\theta}{2}\sqrt{\tan^2\frac{\theta}{2} + \frac{Q^2}{q^2}}$$

$$v_{TL}' = -\frac{Q^2}{q^2}\frac{\tan\frac{\theta}{2}}{\sqrt{2}}$$

Here $q^2 = Q^2 + \nu^2$ is the conventional notation. By varying θ^*, the angle between the nuclear spin and the direction of momentum transfer, it is possible to pick out the longitudinal and transverse pieces of the quasi–elastic spin–dependent cross section. In particular, if $\theta^* = 90°$, then the asymmetry, $A_\perp$, is proportional to G_E^n/G_M^n. This reflects

the power of the spin degree of freedom to pick out the interesting pieces of the cross section.

In case the polarization asymmetry is measured using vector polarized deuterium, it will be necessary to measure the recoil neutron in coincidence with the scattered electron to veto against much larger asymmetry effects from the polarized proton in the deuteron. Model calculations[12,13] show that the polarization asymmetry is linearly dependent on G_E^n/G_M^n as long as the recoil neutron is emitted at small angles with respect to the direction of the virtual photon. In this region the influence of the deuteron wave function on the extracted value of G_E^n/G_M^n is almost absent (Figures 17 and 18). At large angles, the asymmetry is very sensitive to specific ingredients of the deuteron wave function and to final state interactions. Measurements in this kinematic region will therefore be of great interest. Figures 17 and 18 also demonstrate that good neutron angular resolution is important to select neutrons near the cross section maxima of the quasi–elastic peaks (0° for quasifree e–p scattering, 180° for quasifree e–n scattering) where the asymmetry is well understood theoretically and most sensitive to G_E^n/G_M^n. To achieve the required sensitivity, the angular resolution should be better than 2°.

For the ideal kinematic setting, the asymmetry A_{en} is only sensitive to the ratio G_E^n/G_M^n. Any practical detection system will use a finite acceptance; it is therefore necessary to study the effect of finite acceptances on the asymmetry. Figure 19 shows the asymmetries A_{en} for neutrons and A_{ep} for protons as a function of Q^2 for 4 GeV incident electrons and an orientation of the nucleon spin of 42° relative to the incident electron. The asymmetries are given for $\phi^* = 0$, but there is little reduction of the asymmetry for a $\pm 20°$ interval in the electron azimuthal angle. The ideal setting is reached for $Q^2 = 1.5$ $(GeV/c)^2$. At this setting, one is performing essentially a null–measurement. The limits for G_E^n/G_M^n are then given by the statistical precision, and, in principle, very low values of G_E^n/G_M^n are detectable. (In practice, it will be difficult to get sufficient count rate to make use of that advantage.) Away from the ideal setting, the asymmetry contains an additive term that depends strictly on kinematics and can therefore be calculated accurately and subtracted. The only practical disadvantage is that the accuracy for G_E^n/G_M^n will now be influenced by the absolute accuracy of the determination of electron and neutron polarization.

Also shown in Figure 19 is the asymmetry for e–p scattering. The asymmetry is generally larger than for e–n scattering. Additionally, the e–p cross section and the detection efficiency for protons are larger, making the simultaneous detection of e–p coincidences a valuable test of the experimental technique. Also, the influence of the binding effects in deuterium can be tested by comparing the asymmetry for free and bound protons using NH_3 and ND_3 polarized targets.

In a large acceptance detector, e–n and e–p coincidences can be recorded simultaneously in the kinematic situation in which the angles of electron and nucleon are reversed (for fixed target spin orientation). The asymmetries, given in Figure 20, are large. As expected, there is practically no sensitivity to G_E^n/G_M^n left. Therefore, this measurement will not only check the experimental procedure but eliminate uncertainties in the determination of the product of beam and target polarization.

The electron solid angle that can be used simultaneously for this experiment (one segment of the CLAS only) is about 100 msr. This is more than one order of magnitude larger than the focussing spectrometers planned for CEBAF. (Using a focussing spectrometer, it is standard procedure to increase the electron beam current for large angle measurements to compensate for the decreasing cross section. Note that this procedure does not work for polarized targets since their luminosity is limited.) Using a large acceptance detector, the solid angle grows with increasing Q^2 (for constant dQ^2/Q^2), a welcome feature in a situation of strongly decreasing cross sections. For 4 GeV incident electrons, the Q^2 range from 0.5–2.5 $(GeV/c)^2$ can be covered simultaneously. (A detailed analysis of the experimental errors may reveal that it will be more appropriate to use two settings of the electron energy, e.g. 2 and 4 GeV.) In addition, the cross section for deuteron electro–disintegration drops very rapidly as one moves away from the quasi–elastic e–p and e–n peaks. For the measurement of the asymmetry for this process a large solid angle device is absolutely necessary.

The ^{14}N component of the target constitutes a serious background that has to be reduced experimentally by kinematic overdetermination. A Monte Carlo calculation was performed to analyze the distribution of quasi–elastic e–n scattering events from deuterium and from ^{14}N. Figure 21 shows missing mass distributions (derived from the difference between incident and outgoing electron assuming a free neutron as a target) without and with neutron detection. With the neutron confined to a narrow (5°) cone around the direction of the virtual photon, the ^{14}N contributions underneath the quasi–elastic deuterium peak can be reduced to about 30%. Note that only the direction of the neutron has been used in the cut. Additional gains may be possible using the time–of–flight information. The Monte Carlo calculation has to be extended to include the electro–disintegration process with nucleons far away from the quasi–elastic peak. In the CLAS detector, kinematic overdetermination can be achieved by the coincident detection of the scattered electron and the proton–neutron pair; this should reduce the nuclear background to negligible levels.

V. Target Polarization Asymmetry in Single Pion Production

The proposal of the N^* group emphasizes the importance of measurements of polarization observables in a program to completely determine the resonance transition parameters. Such a program requires measurement of single π and η production. The coincidence cross section for single hadron detection can be written as:

$$\frac{d\sigma}{d\Omega_e dE_e d\Omega_h} = \Gamma_T \frac{d\sigma}{d\Omega_h} \quad ; \quad \frac{d\sigma}{d\Omega_h} = \sigma_o + \sigma_e + \sigma_t + \sigma_{et}$$

where, for simplicity, we have omitted the $\frac{d}{d\Omega}$. σ_o, σ_e, σ_t, and σ_{et} represent the unpolarized cross section, and terms related to the electron polarization, nucleon polarization, and combined electron and nucleon polarization.

σ_o, σ_e, σ_t, σ_{et} contain 4, 1, 8, and 5 response functions, respectively. These can be determined at any given kinematical point in W, Q^2, θ_h, by measuring the ϕ, and ϵ dependence of the cross section. The response functions can be expressed in terms of 6 parity conserving helicity amplitudes (we have used the notation of Bartl and Majerotto [18]

for the helicity amplitudes). A complete determination of the helicity amplitudes is seen as a long term goal in single π electroproduction, which would allow an essentially model–independent extraction of the resonant transition amplitudes. It requires measurement of at least 11 independent quantities, not taking into account an undefined overall phase.

V.1 Unpolarized Measurements.

Experiments which measure no polarization observables allow the determination of the following 3 terms if the ϕ dependence is measured only:

$$|h_+^N|^2 + |h_+^F|^2 + |h_-^N|^2 + |h_-^F|^2 + \epsilon \cdot (|h_o^N|^2 + |h_o^F|^2)$$

$$|h_-^N|^2 + |h_-^F|^2 - |h_+^N|^2 - |h_+^F|^2$$

$$Re(h_o^N h_-^{N*} + h_o^F h_-^{F*})$$

V.2 Polarized Electron Beam

Using a polarized electron beam with an unpolarized target allows the determination of the term

$$Im(h_o^N h_-^{N*} + h_o^F h_-^{F*})$$

V.3 Target Polarization at an Angle to the Electron Beam

For the case that the target is polarized, and the polarization can be aligned along any given axis in the horizontal plane, measurement of the ϕ distribution allows the determination of the following terms:

$$Im(h_o^F h_+^{N*} + h_o^N h_+^{F*})$$

$$Im(h_-^F h_+^{N*} + h_-^N h_+^{F*})$$

$$Im(h_+^N h_+^{F*} + h_-^N h_-^{F*}) + 2\epsilon Im(h_o^N h_o^{F*})$$

$$Im(h_-^N h_-^{F*} + h_+^N h_+^{F*})$$

$$Im(h_o^N h_-^{F*} - h_o^F h_-^{N*})$$

$$Im(h_o^N h_+^{N*} - h_o^F h_+^{F*})$$

$$Im(h_-^N h_+^{N*} - h_-^F h_+^{F*})$$

With a polarized electron beam and a polarized nucleon target one measures the bilinear combinations:

$$Re(h_o^F h_+^{N*} + h_o^N h_+^{F*})$$

$$Re(h_-^F h_+^{N*} + h_-^N h_+^{F*})$$

$$Re(h_o^N h_-^{F*} - h_o^F h_-^{N*})$$

$$Re(h_o^N h_+^{N*} - h_o^F h_+^{F*})$$

$$Re(h_-^N h_+^{N*} - h_-^F h_+^{F*})$$

Together with the unpolarized measurements 16 response functions, or combinations of response functions can be determined by analyzing the ϕ distribution of the cross section and polarization asymmetries, without varying ϵ. Variation of ϵ would allow separation of all 18 response functions.

V.4 Target Polarized Parallel to the Beam Direction

For the case that the target is polarized along the direction of the electron beam, the following combinations can be measured by varying ϕ only (θ_γ is the lab angle of the virtual photon).

$$Im(h_+^N h_+^{F*} + h_-^N h_-^{F*}) + \epsilon \cdot [Im(h_-^N h_-^{F*} - h_+^N h_+^{F*}) + 2 \cdot Im(h_o^N h_o^{F*})]$$

$$+ cos\theta_\gamma \sqrt{2\epsilon(1+\epsilon)} Im(h_o^N h_+^{N*} - h_o^F h_+^{F*}) \ ;$$

$$-\frac{1}{2} sin\theta_\gamma \sqrt{2\epsilon(1+\epsilon)} [Im(h_o^F h_+^{N*} + h_o^N h_+^{F*}) + Im(h_o^N h_-^{F*} - h_o^F h_-^{N*})] +$$

$$cos\theta_\gamma \cdot \epsilon \cdot Im(h_-^N h_+^{N*} - h_-^F h_+^{F*}) \ ;$$

$$Im(h_-^F h_+^{N*} + h_-^N h_+^{F*}) - 2Im(h_-^N h_-^{F*} + h_+^N h_+^{F*}) \ .$$

If both, beam and target are polarized along the beam axis, the following terms can be determined:

$$Re(h_o^N h_-^{F*} - h_o^F h_-^{N*}) + \sqrt{2\epsilon(1-\epsilon)} Re(h_o^F h_+^{N*} + h_o^N h_+^{F*}) \ ,$$

$$sin\theta_\gamma \sqrt{1-\epsilon^2} Re(h_-^F h_+^{N*} + h_-^N h_+^{F*}) - cos\theta_\gamma \sqrt{2\epsilon(1-\epsilon)} Re(h_o^N h_+^{N*} - h_o^F h_+^{F*}) \ ,$$

$$sin\theta_\gamma Re(h_o^N h_-^{F*} - h_o^F h_-^{N*}) + cos\theta_\gamma \sqrt{1-\epsilon^2} Re(h_-^N h_+^{N*} - h_-^F h_+^{F*}) \ .$$

Together with the unpolarized measurements 10 response functions, or combination of response functions can be determined by analyzing the ϕ distribution of the unpolarized cross section and the various polarization asymmetries, without varying ϵ. Variation of ϵ would allow measurements of 16 combination of bilinear terms. In practice, however, this may be difficult to achieve because of the relatively weak sensitivity to ϵ variations.

One can show that with only two more (appropriately chosen) measurements a complete determination of all 6 complex helicity amplitudes can be accomplished, which demonstrates that even in a non-optimal configuration (target and beam polarized along

the beam direction), polarization measurement will generate very significant information on baryon resonance excitation which cannot be obtained in unpolarized measurements.

VI. Target Asymmetry in the Region of the Roper.

Measurements of single π and η production from a polarized hydrogen or deuterium target have never been done before. Such experiments would mark a significant improvement in the study of the structure of excited nucleons. In the following, one particularly interesting example is briefly discussed, which demonstrates the power of the use of polarized targets in these experiments.

The Roper resonance or $P_{11}(1440)$ is a well established nucleon resonance, and its coupling to real photons has been extracted with small uncertainties from single π photoproduction experiments. In electron scattering experiments, however, this resonance has hardly been seen, and there is only one recent analysis[14] of older DESY and NINA data at Q^2=1GeV which produced stable results for its excitation. These results, however, are somewhat contradictory as far as the excitation by transverse photons is concerned, but they do agree in the surprising result that the $P_{11}(1440)$ couples strongly to longitudinal photons. This, in fact, is the only resonance for which an appreciable longitudinal coupling has been found, and it is interesting to note that in the mass region of the P_{11} indications of a stronger longitudinal component than elsewhere in the resonance region were also found in an independent analysis of inclusive data[15].

Quark model calculations, which generally reproduce the photon coupling amplitudes, are barely able to predict the correct sign of the P_{11} transverse amplitude. However, a large longitudinal photocoupling amplitude has been predicted recently within the framework of a relativized quark potential model[16]. Obviously, the only way to come to a better understanding of the structure of this resonance, is to perform measurements that are more sensitive to small amplitudes such as expected for the electromagnetic coupling of the Roper in electron scattering.

Use of polarized targets in CLAS provides a powerful tool for such a measurement. Although a systematic experimental exploration would cover the entire resonance region and a large Q^2 range, it is instructive to evaluate one specific kinematical situation, which uses a polarized proton (NH_3) target. Useful quantities to measure with a polarized spin–1/2 target are the target asymmetries, defined as

$$T_i = \frac{\sigma(P_i = +1) - \sigma(P_i = -1)}{\sigma(P_i = +1) + \sigma(P_i = -1)}$$

where i = x, y, z, (or long). P_x, P_y, P_z are the polarization components in the $N\pi$ decay plane, perpendicular to the $N\pi$ decay plane, and in the direction of the virtual photon, respectively (P_{long} is the target polarization when the target is polarized along the beam direction).

Figure 22 displays the cross section for single π^o production as predicted by the Kroesen analysis [14] with and without the Roper resonance included in the computation of the

cross section. The differences are very small. It would be very difficult to extract the small signal coming from the Roper excitation. Figure 23 displays the polarized target asymmetry T_x for the same kinematics as in Figure 22, and Figure 24 shows the angular distribution of the asymmetry. Obviously, the effects are much larger than in the unpolarized cross section. To see whether the effect can be mocked up by modifications of the amplitudes of other nearby resonances, the asymmetry is plotted with the $S_{11}(1535)$ transition amplitudes set to zero. Note that the S_{11} amplitudes are, in fact, known at the 20% level[17]. Modifications within this uncertainty would clearly not affect the sensitivity of T_x with respect to the P_{11}. Measurement of the polarized target asymmetry $T_x(\phi = 90°)$ in the region of the $P_{11}(1440)$ would allow one to place strong constraints on the excitation strength of this resonance.

We now address in some more detail measurements of polarized target asymmetries in the region of the $P_{11}(1440)$ resonance when the target is polarized along the beam direction. Such a configuration might be implemented for the first round of polarized target experiments. The target asymmetry T_{long} can be predicted using the Kroesen amplitudes for π^o production. Some results are shown in Figure 25 and Figure 27 for specific kinematics. Also shown is the sensitivity to variations of some contributing amplitudes. Obviously, this asymmetry is very sensitive to various assumptions about the Roper amplitudes.

In the following we estimate the statistical accuracy for measuring the T_{long} asymmetry in π^o production off polarized protons. The unobstructed opening angle of the target magnet is large enough to essentially allow detection of protons in nearly the full phase space of the reaction. This is possible because the protons are confined in a cone around the direction of the virtual photon with an opening angle which is small enough, so that nearly all protons for the specific kinematics of the Roper $P_{11}(1440)$ excitation can be detected in CLAS (of course, there will be some obstruction of acceptance due to the CLAS magnet geometry, similar to the unpolarized case). Figure 29 shows, as an example, the proton kinematics for $Q^2 = 1.GeV^2$.

The count rates are estimated based on the following assumptions:

Free Proton Polarization P_p=0.7

Effective Polarization $P_p^{eff} = 0.5$

Luminosity=$10^{34}cm^{-2}sec^{-1}$ (for free protons)

Beam Energy $E_e = 4GeV$

Bin sizes:$\Delta W = 20 MeV, \Delta cos\theta^* = 0.166, \Delta Q^2 = 0.2 GeV^2$

Running time = 1000 hrs

The reduction in P_p^{eff} compared to P_p is the result of contributions from the ^{14}N. The estimated statistical uncertainties are shown in Figure 26 and Figure 28. Obviously, the measurements will generate data that would significantly constraint the analysis in term of the resonant amplitudes in the Roper region. Equally important information on the nonresonant amplitudes will be obtained as well. In addition, the measurements

will generate data over a very large kinematical area in Q^2, W, and $\cos\theta^*$. Moreover, equally important π^+ data will be obtained in a large kinematical region. The combined polarized target data on π° and π^+ production would improve the data base for single pion electroproduction in a very significant way, providing experimental information necessary for a model independent analysis of electromagnetic baryon excitation.

In case polarized electron beams are available, double polarization asymmetries can be measured. Measurements of this type provide information which is complementary to the polarized target asymmetries, and is needed for a complete understanding of the electromagnetic couplings of baryons. Note that the double polarization asymmetries contain only real parts of combination of amplitudes, whereas the target asymmetries contain only imaginary parts. In Figure 30 and Figure 31 predicted double polarization asymmetries for π^+ are shown using the Kroesen amplitudes. Obviously, the double polarization asymmetries are equally sensitive to the various resonant and non-resonant amplitudes.

VII. Conclusions

Experiments in electromagnetic nuclear physics concentrate more and more on relatively small (but important) phenomena that are more readily accessible via interference effects. Measurements of this type often require the use of polarized beams and polarized targets. The luminosity limitation that hampers the use of these targets can be overcome by combining them with a large acceptance spectrometer. The properties of the CEBAF Large Acceptance Spectrometer are ideally matched to the properties of polarized targets. Both devices are complicated; teaming them up should wait till both are well understood. However, it is important to plan these experiments now to make sure that there will be no surprises in the future.

References

[1] T.W. Donnelly and A.S. Raskin, Annals of Physics **169**, 247 (1986)

[2] T.W. Donnelly, 1985 CEBAF Summer Workshop, p. 57

[3] R.G. Milner *et al.*, Nucl. Instr. and Meth.

[4] T.E. Chupp *et al.*, Phys. Rev. **C57**, 2244(1987)

[5] W. Meyer, 1985 CEBAF Summer Workshop, p. 237

[6] Proceeding 4th International Workshop on Polarized Target Materials and Techniques, Bad Honnef, September 1984

[7] V.E. Krohn and G.R. Ringo, Phys. Rev. **148**, 1303 (1966); Phys. Rev. **D8**, 1305 (1973)

[8] S. Galster *et al.*, Nucl. Phys. **B32**, 221 (1971)

[9] M. Gari and W. Krumpelmann, Z. Phys. **A322**, 689 (1985), Phys. Lett. **B173**, 10 (1986)

[10] J.G. Korner and M. Kuroda, Phys. Rev. **D16**, 2165 (1977)

[11] R.G. Arnold *et al.*, Phys. Rev. **C23**, 363 (1981)

[12] H. Arenhovel *et al.*, Z. Phys. **A331**, 123 (1988)

[13] M.P. Rekalo *et al.*, Proc. of the International Symposium on High Energy Spin Physics, Protvino (USSR) 1986, p. 155

[14] G. Kroesen and B. Boden, Research Program at CEBAF II, Report of the Summer Study Group, 1986. Eds.: V. Burkert et al.

[15] J. Drees *et al.*, Z. Phys. **C7**, 183(1981)

[16] M. Warns *et al.*, BONN–ME–89–04/07 (1989), to be published in Z. Phys.

[17] F. Foster and G. Hughes, Rep. Prog. Phys. **46**, 1445 (1983)

[18] CLAS Preliminary Conceptual Design Report, CEBAF 1989.

[19] A. Bartl, W. Majerotto; Nucl.Phys.**B62**, 267 (1973).
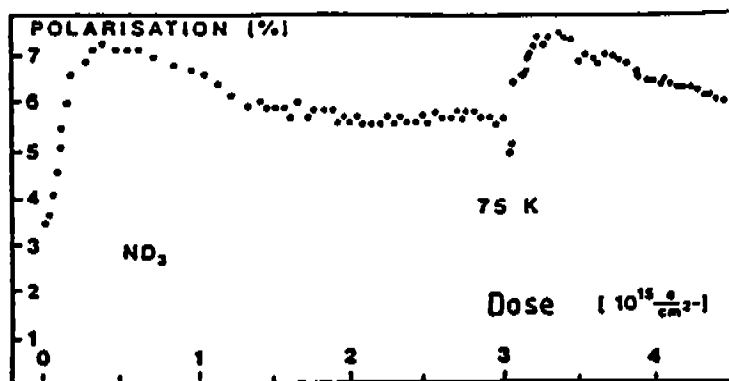
Figure 1 Change of the maximum polarization of ammonia and butanol under irradiation with 1.5 GeV electrons. The target sample was initially pre–irradiated at 80 Kelvin with 10^{17} electrons/cm^2.
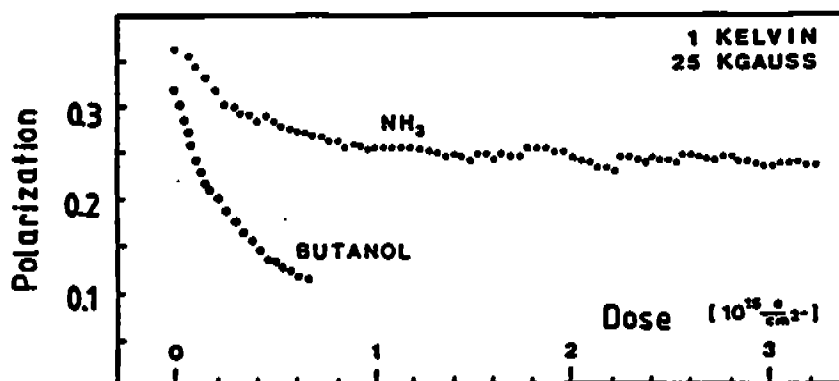
Figure 2 Annealing performance of irradiated ammonia.
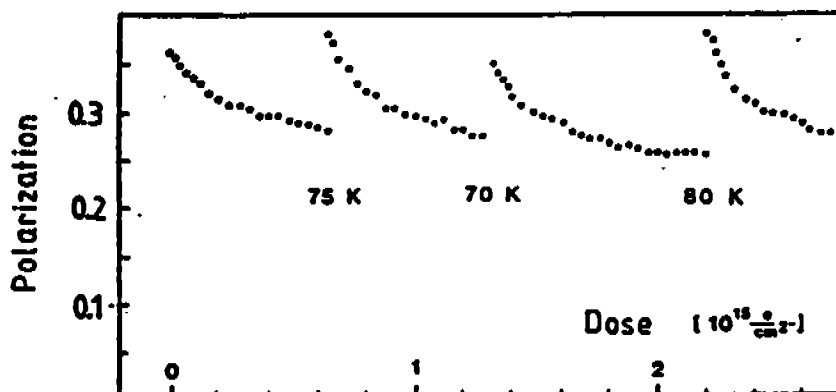
Figure 3 Change of the maximum polarization of deuterated ammonia irradiated with 1.5 GeV electrons and its annealing performance. The target sample was pre–irradiated at 80 K with 10^{17} electrons/cm^2.
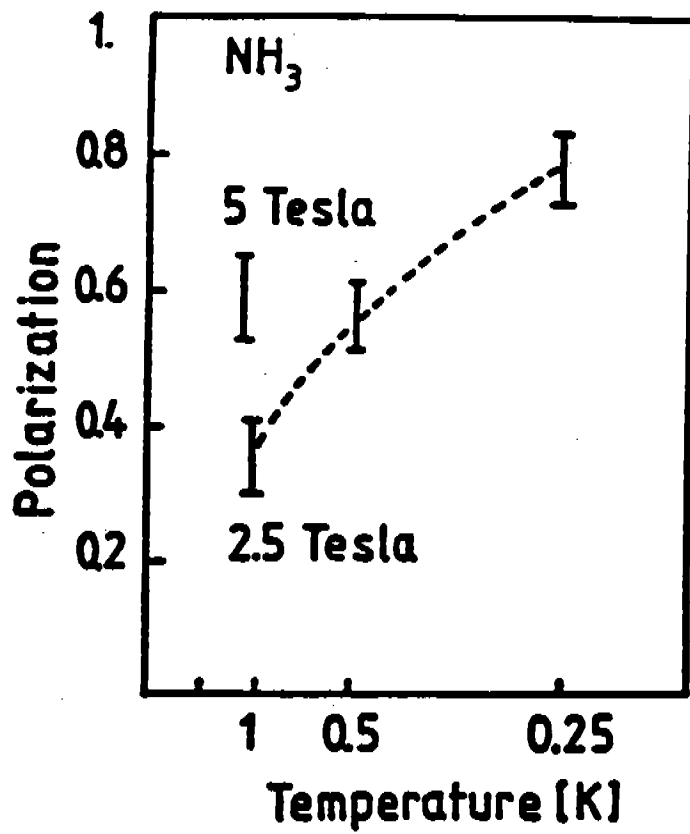
Figure 4 Proton polarization at working temperatures of 250mK, 500mK, and 1000mK.
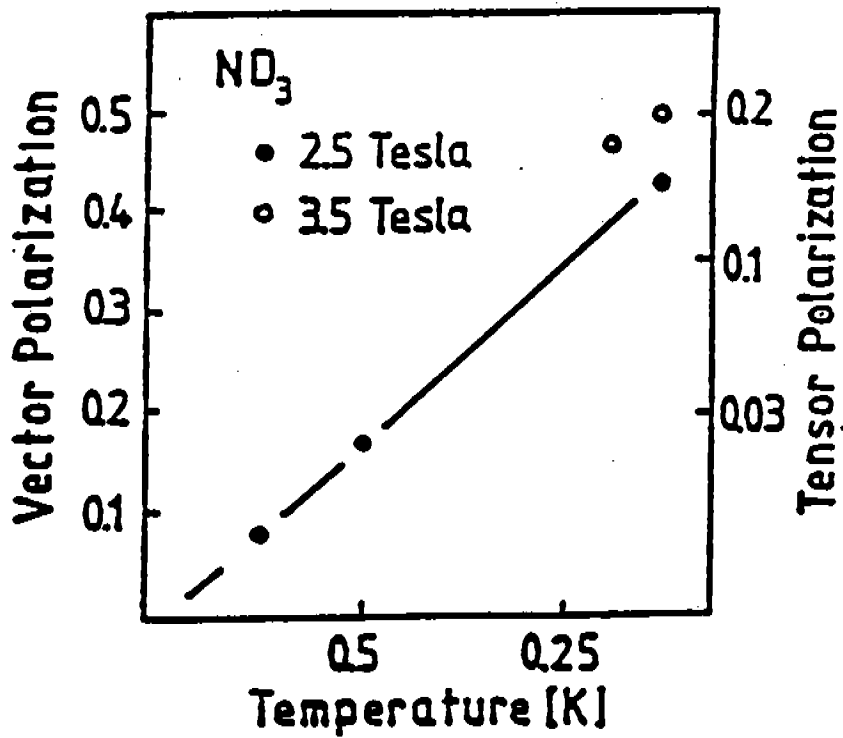
Figure 5 Deuteron polarization in deuterated ammonia versus target temperature.
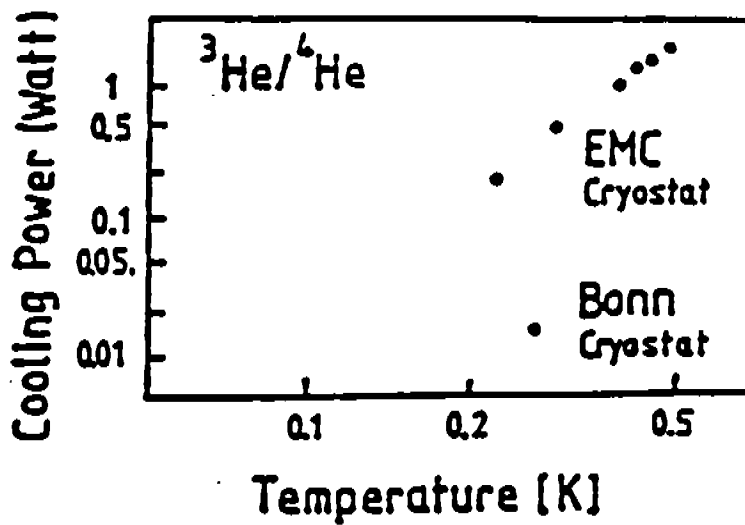
Figure 6 Measured cooling power of CERN cryostat for the EMC experiment and of the Bonn polarized target.
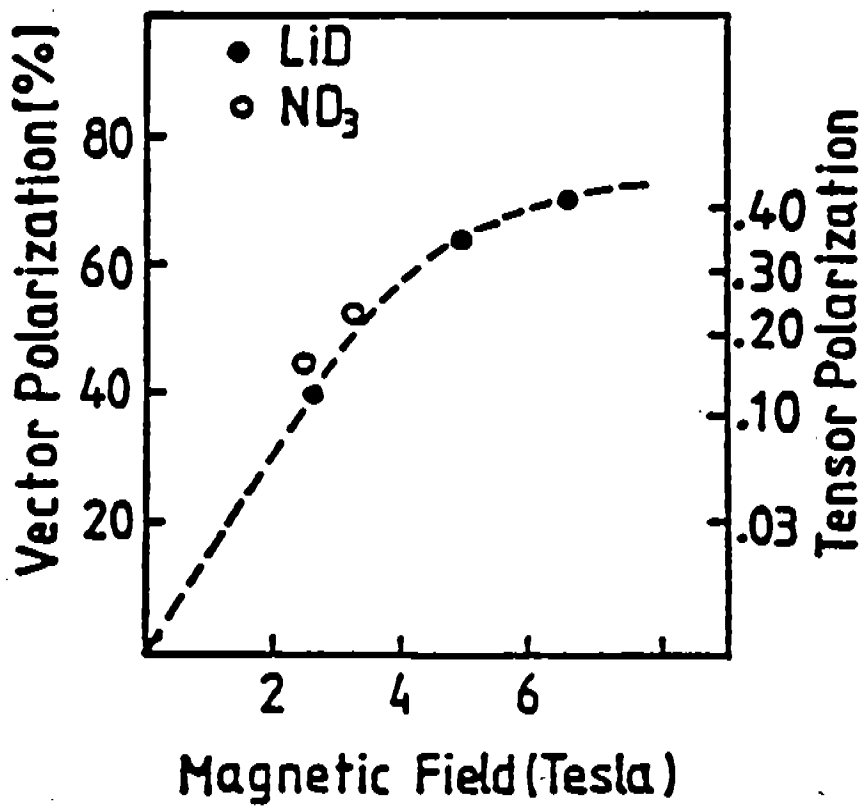
Figure 7 Deuteron polarization versus magnetic field strength for two target materials. (The line is only to guide the eyes.)
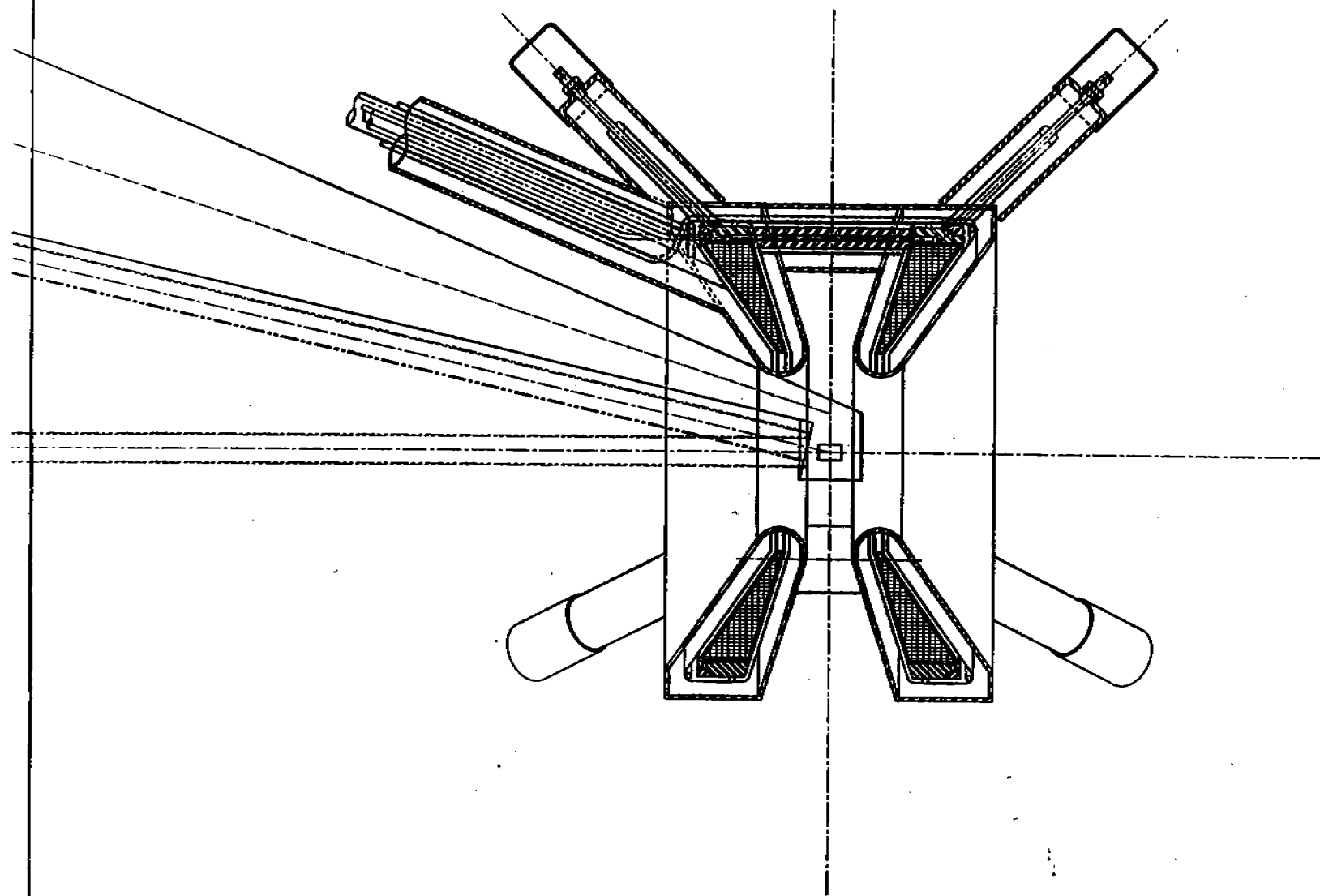
Figure 8 Superconducting split-pair magnet with the coil shape designed for minimal solid angle obstruction and maximum field homogenity.
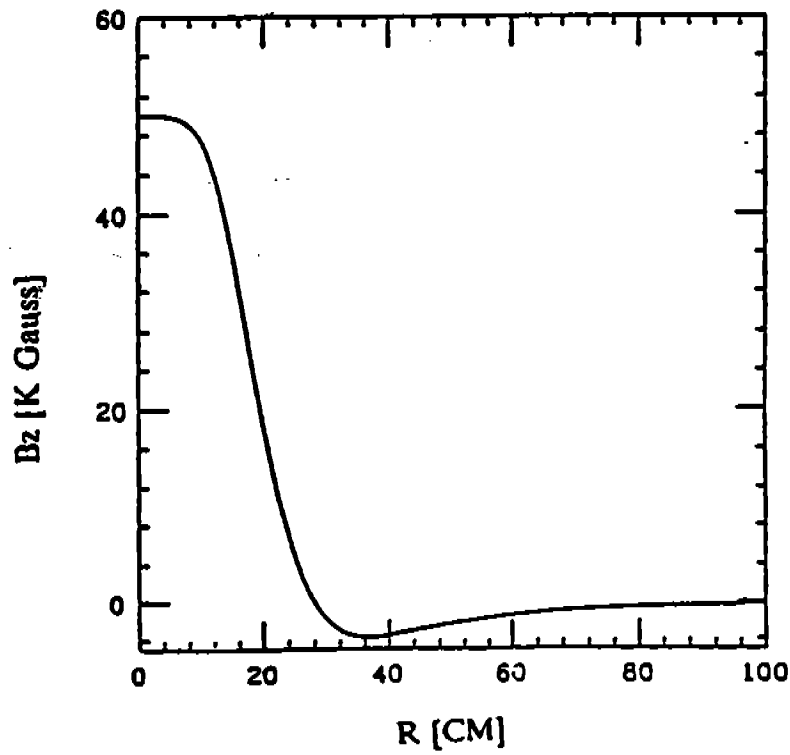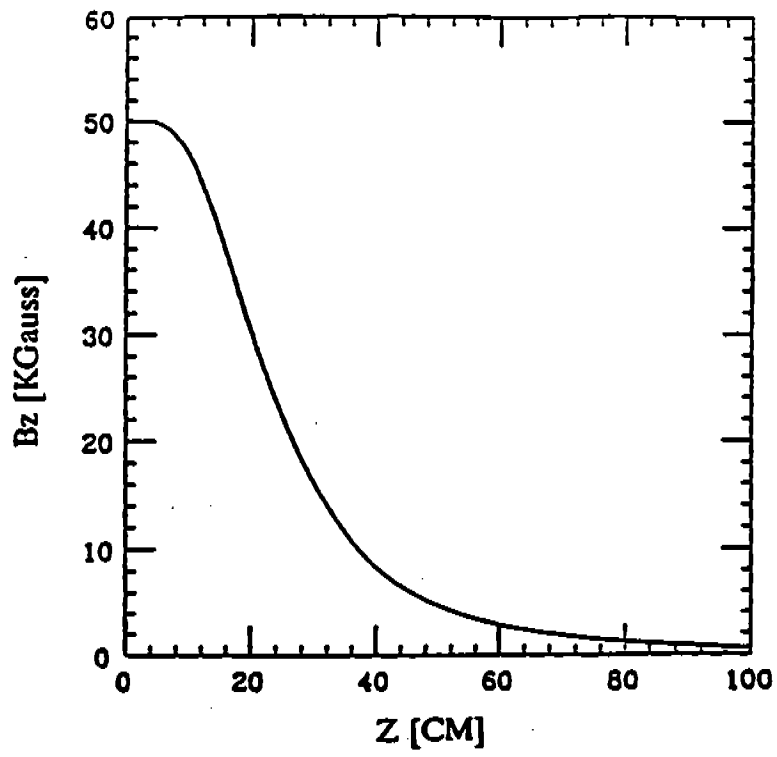
Figure 9 Radial and axial magnetic field distribution of the split pair coil arrangement.

100 cm
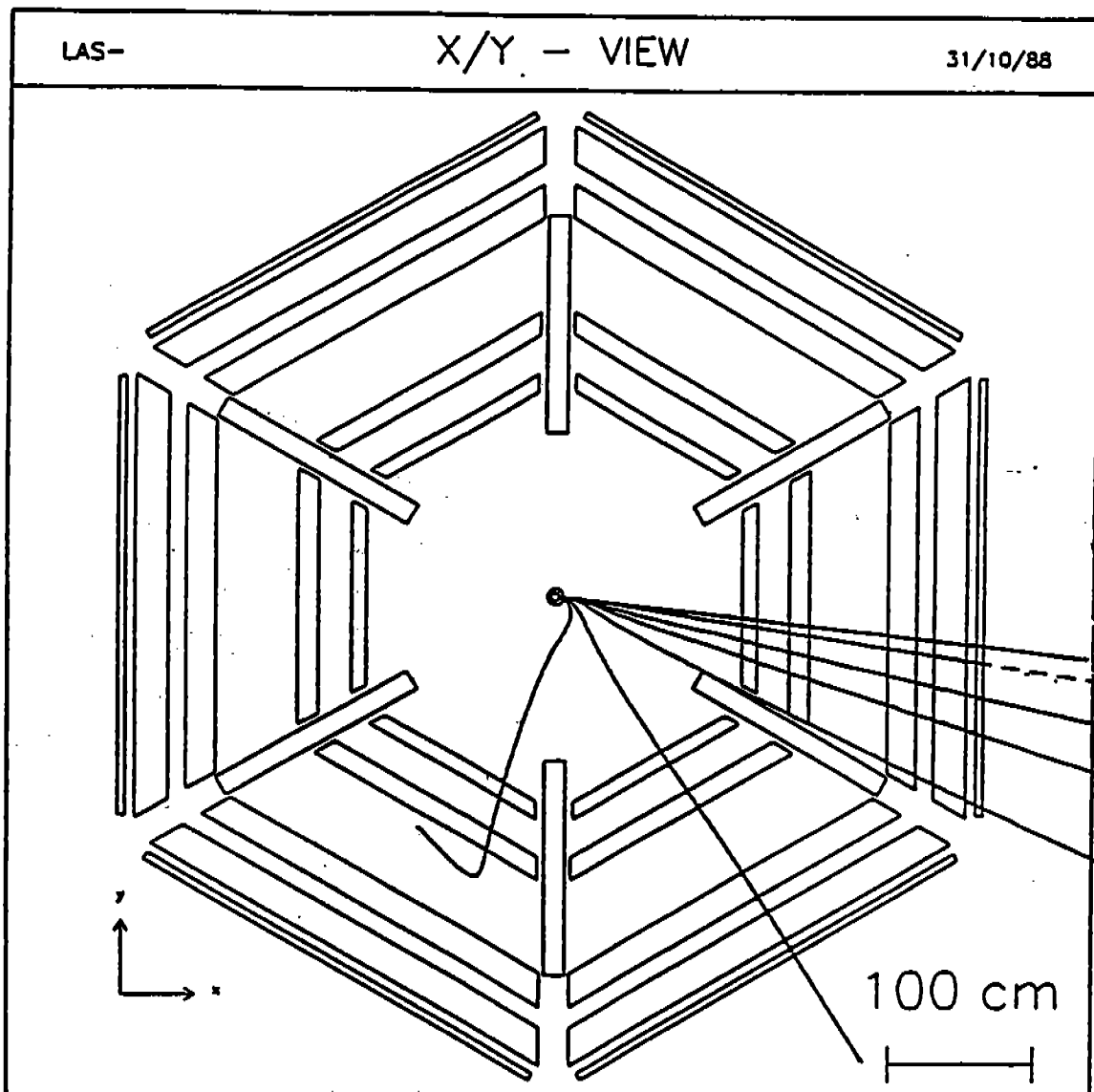
Figure 10 Charged particle trajectories through the target magnet and through the CLAS torus, for momenta between 150, 250, 500, 750, 1000, 1500, and 2000MeV/c.
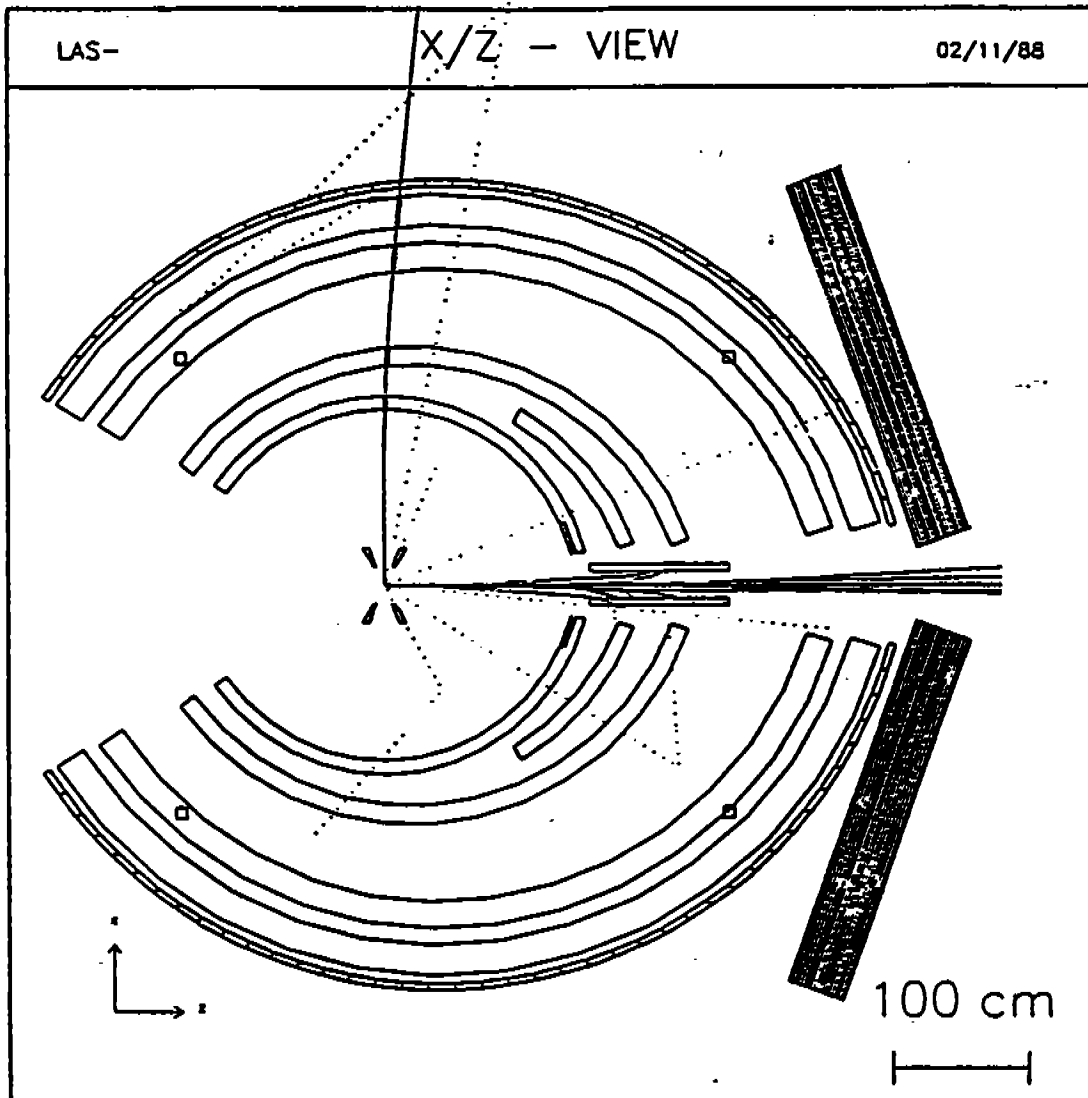
Figure 11 Charged particle background trajectories when the field axis is aligned with the beam direction.
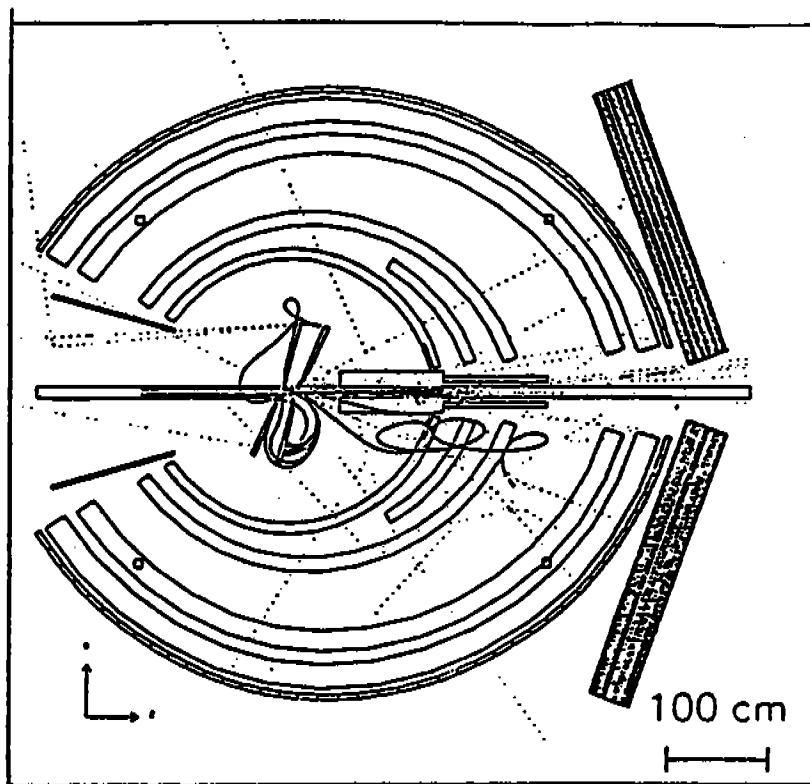
Figure 12 Charged background trajectories when the target field is oriented at a 20°
angle with respect to the beam axis.
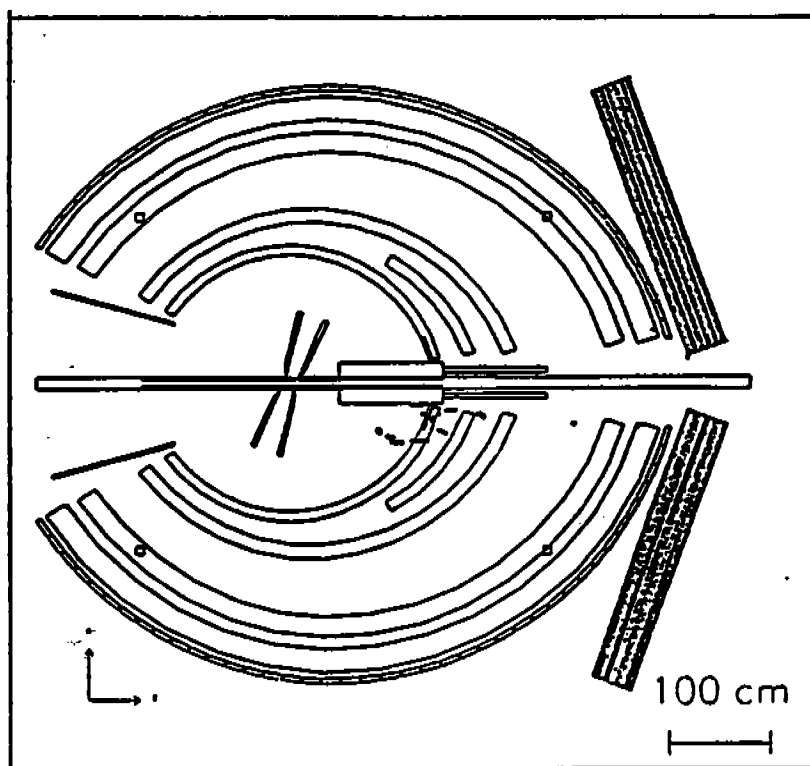
Figure 13 Background hits in the CLAS drift chamber for the arrangement of Figure 12.

LHe & LH2 FEED CAN
CLAS TORUS ASSY (REF)

LHe & LH2 FEED CAN ASSY
& DELIVERY TUBE ASSY

ELECTRON BEAM TUBE at -13.0°
OUT-OF-PLANE (MAX) (REF)

13.0° (MAX)

CRYOGENIC POLARIZED
TARGET ASSY (REF)

ELECTRON BEAM TUBE at 0.0°

CLAS TORUS ASSY
(REF)

POLARIZED TARGET
SOLENOID MAGNET

ATTACHMENT RING WELDMENT (REF)
(.25 (304) STAINLESS STEEL PLT,
ROLLED INTO TRUNCATED CONE)

CLAS TORUS ASSY (REF)
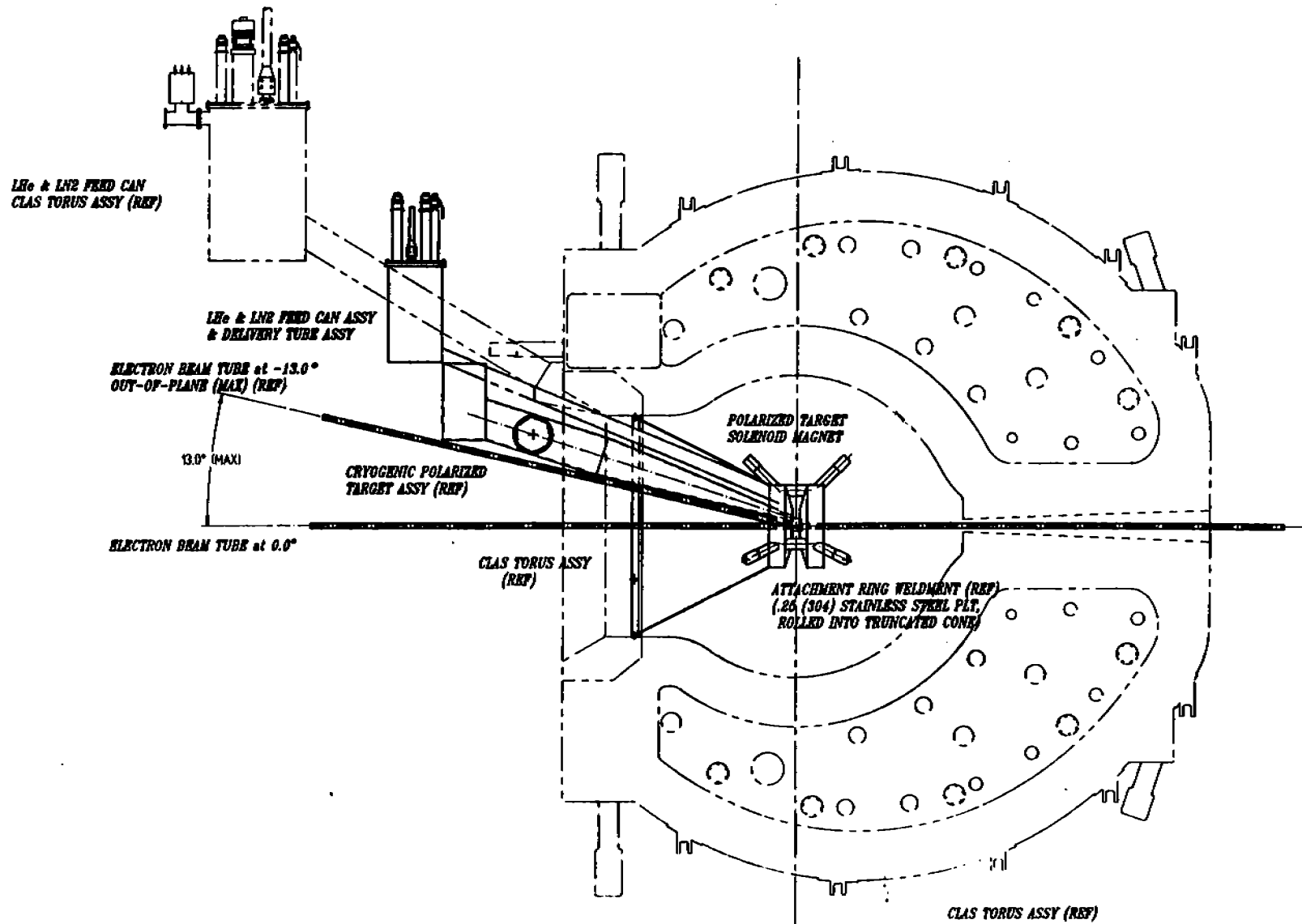
Figure 14 Layout of the polarized target magnet, target cryostat, and support structure in the CLAS magnet.
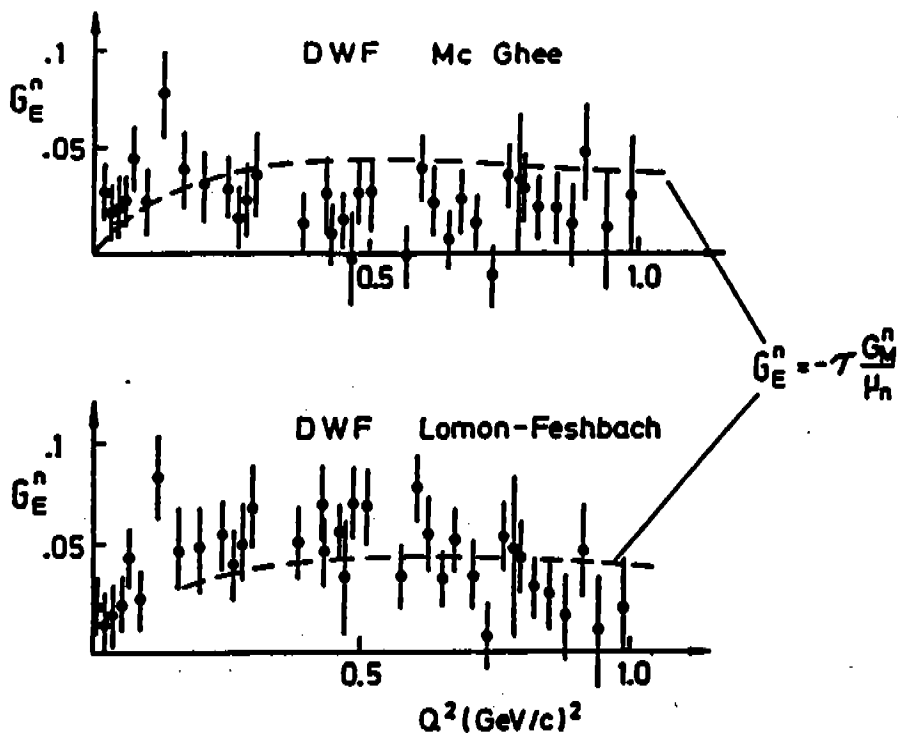
Figure 15 Neutron electric form factor as extracted from elastic electron–deuteron scattering (ref. 8). Note that the different results obtained with the three models of the deuteron indicate a large systematic error.
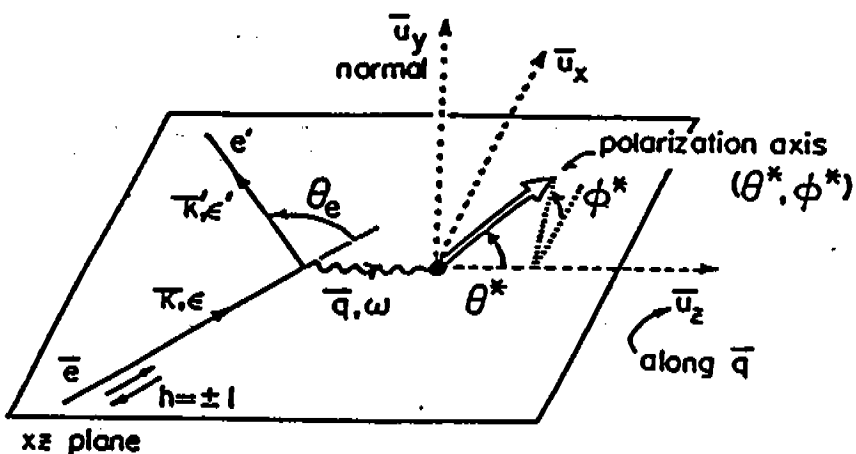
Figure 16 Relevant geometry of the kinematic vectors and spin vectors for inclusive spin–dependent electron scattering (ref. 2).
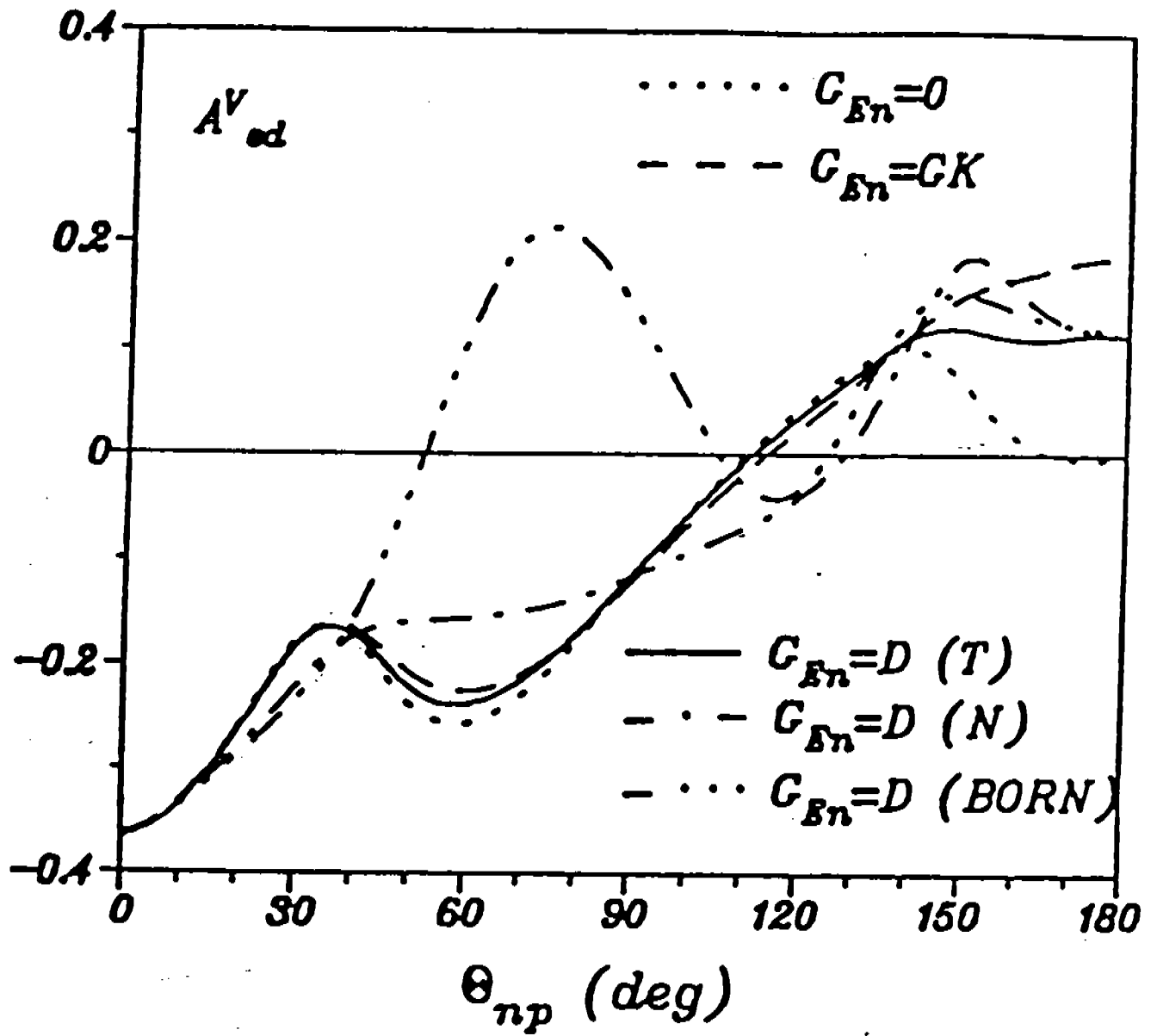
Figure 17 Asymmetry for E_{np}=120 MeV, Q^2=12 fm^{-2} for the Paris potential without (dotted) and with (dashed) final state interaction (N), N + IC (dash–dot), N + MEC (dash–dot–dot), N + IC + MEC (solid). (Ref. 11).
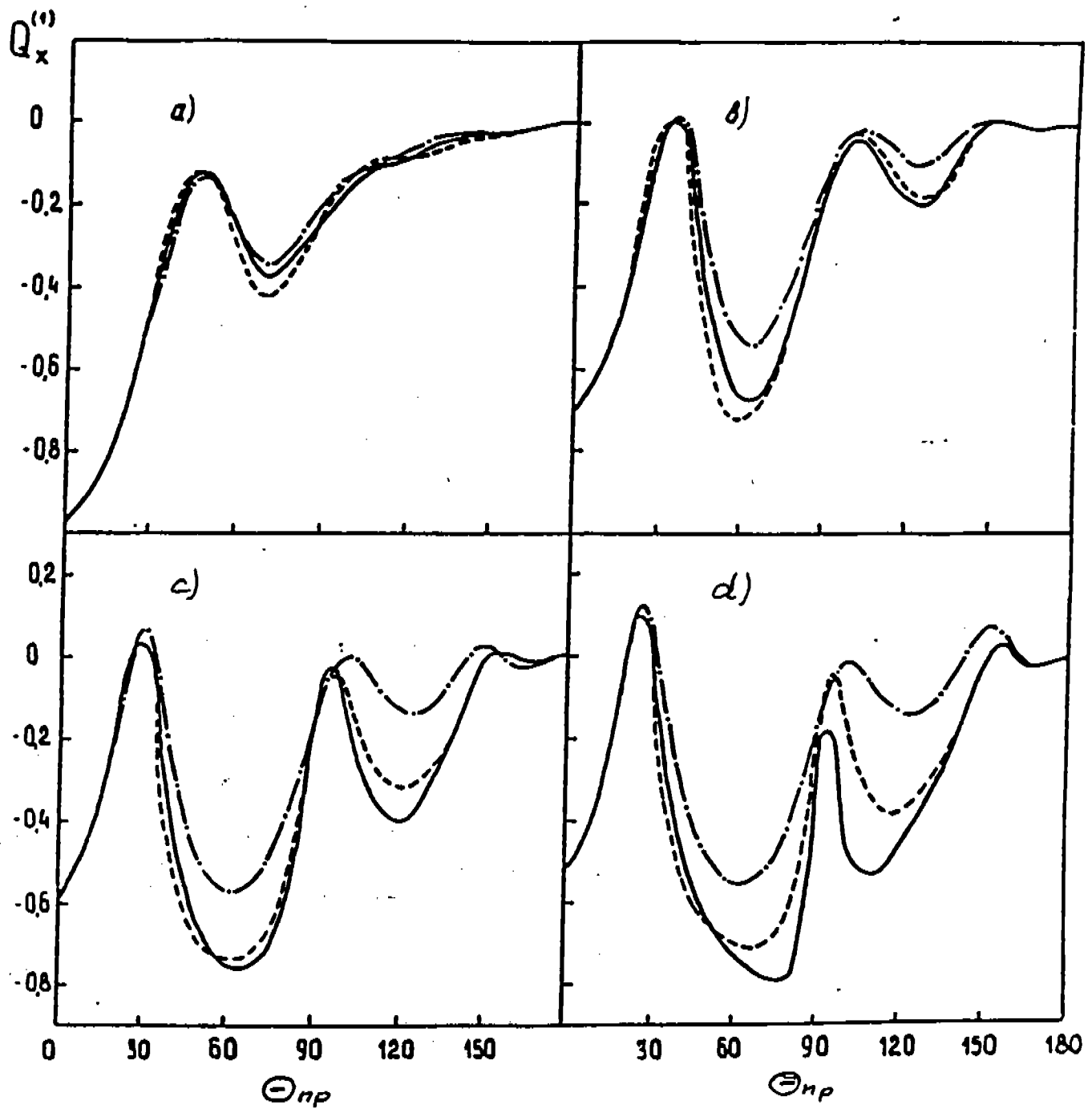
Figure 18 Asymmetry for different choices of the deuteron wave function ($G_E^n = 0$). Solid curve: Paris potential, dashed: Reid SC, dash–dot: Buck–Gross. $Q^2 = 0.5$ (GeV/c)^2 for a), 1.0 for b), 1.5 for c), and 2.0 for d). (Ref. 12).
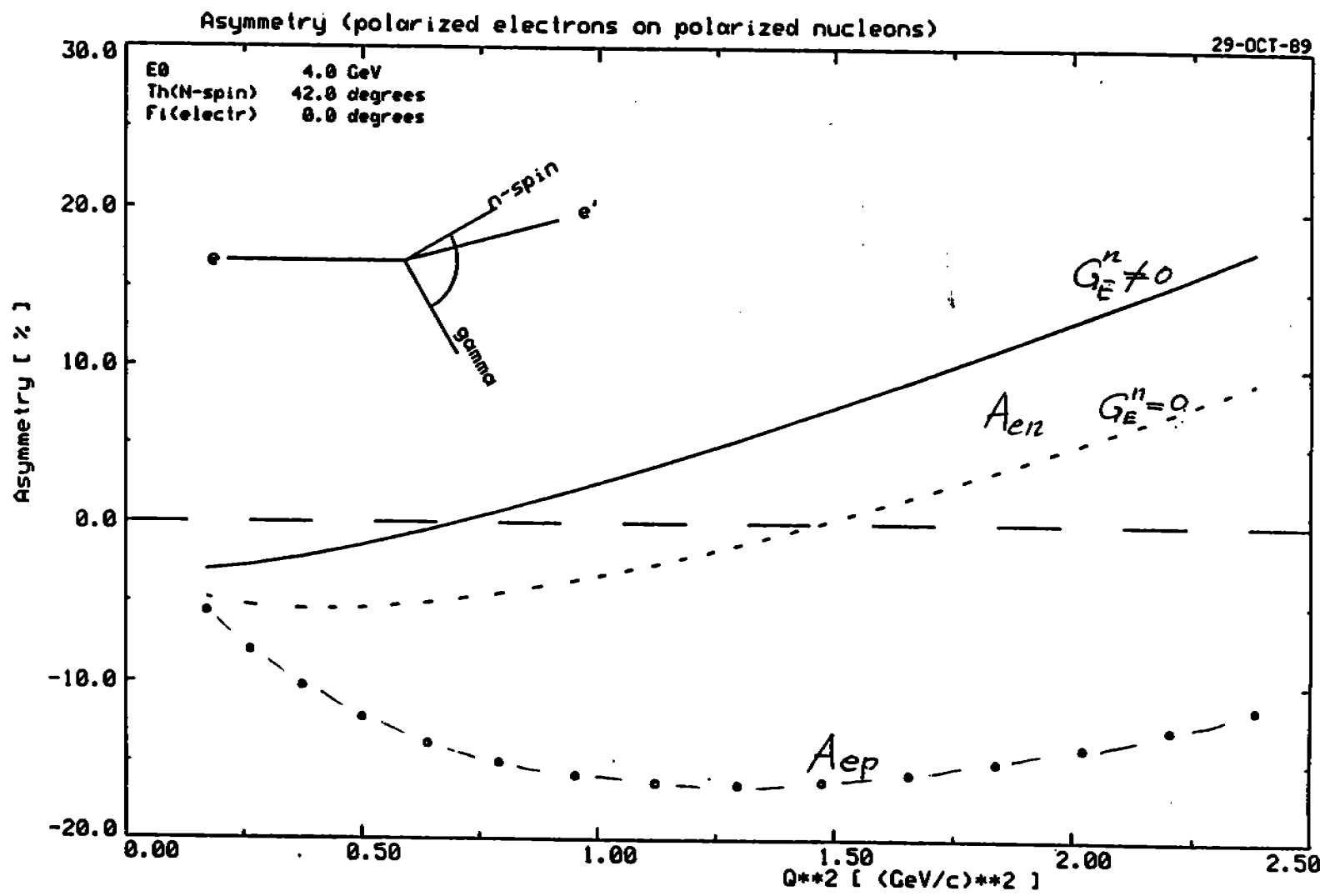
Figure 19 Calculated asymmetries A_{en} for neutrons and A_{ep} for protons as a function of Q^2 for 4 GeV incident electrons and a fixed orientation of the nucleon spin of 42° relative to the incident electron.
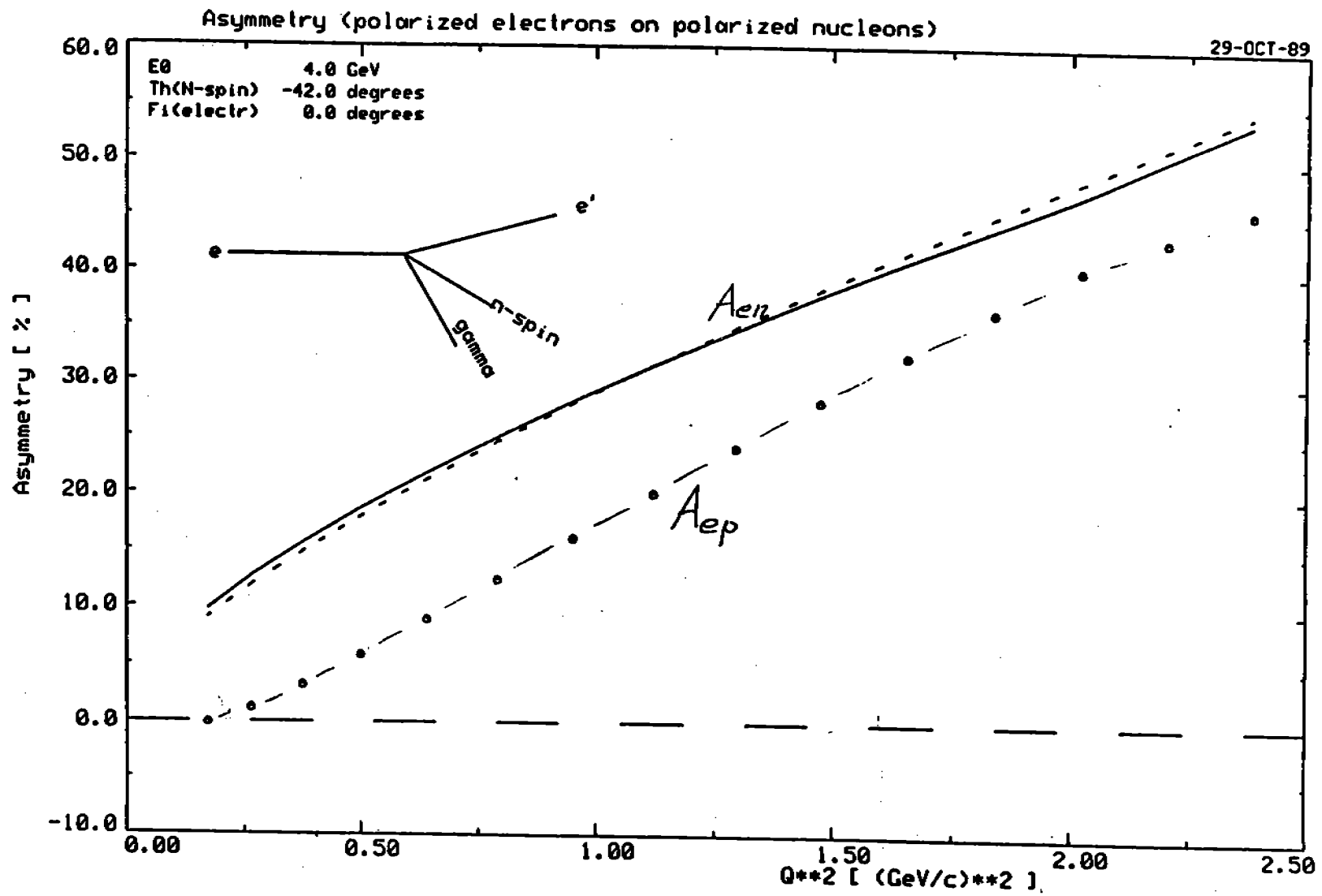
Figure 20   Same as Fig. 9 with the nucleon spin oriented at –42°.
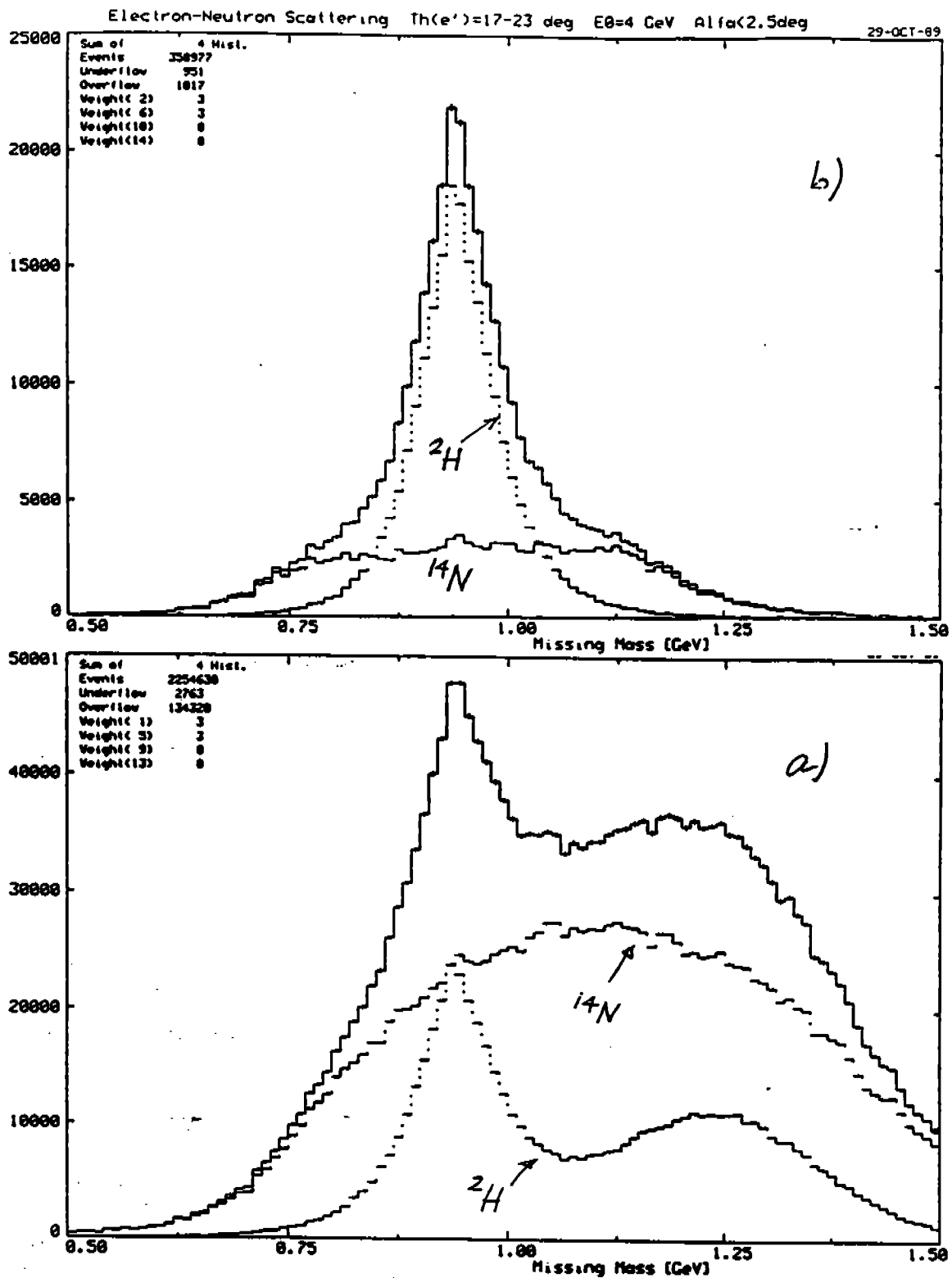
Figure 21 Monte Carlo calculation for the missing mass distributions for quasi–elastic scattering off deuterium and ^{14}N at an incident energy of 4 GeV. Electron scattering angle $17°-23°$. a) no neutron detection, b) neutron detected within a cone around the direction of the virtual photon with a $5°$ opening angle.

Electroproduction: π^o at $Q^2=1.0$ GeV^2/c^2

$\epsilon=0.8$, $\phi=90°$, $\theta^*=0°$
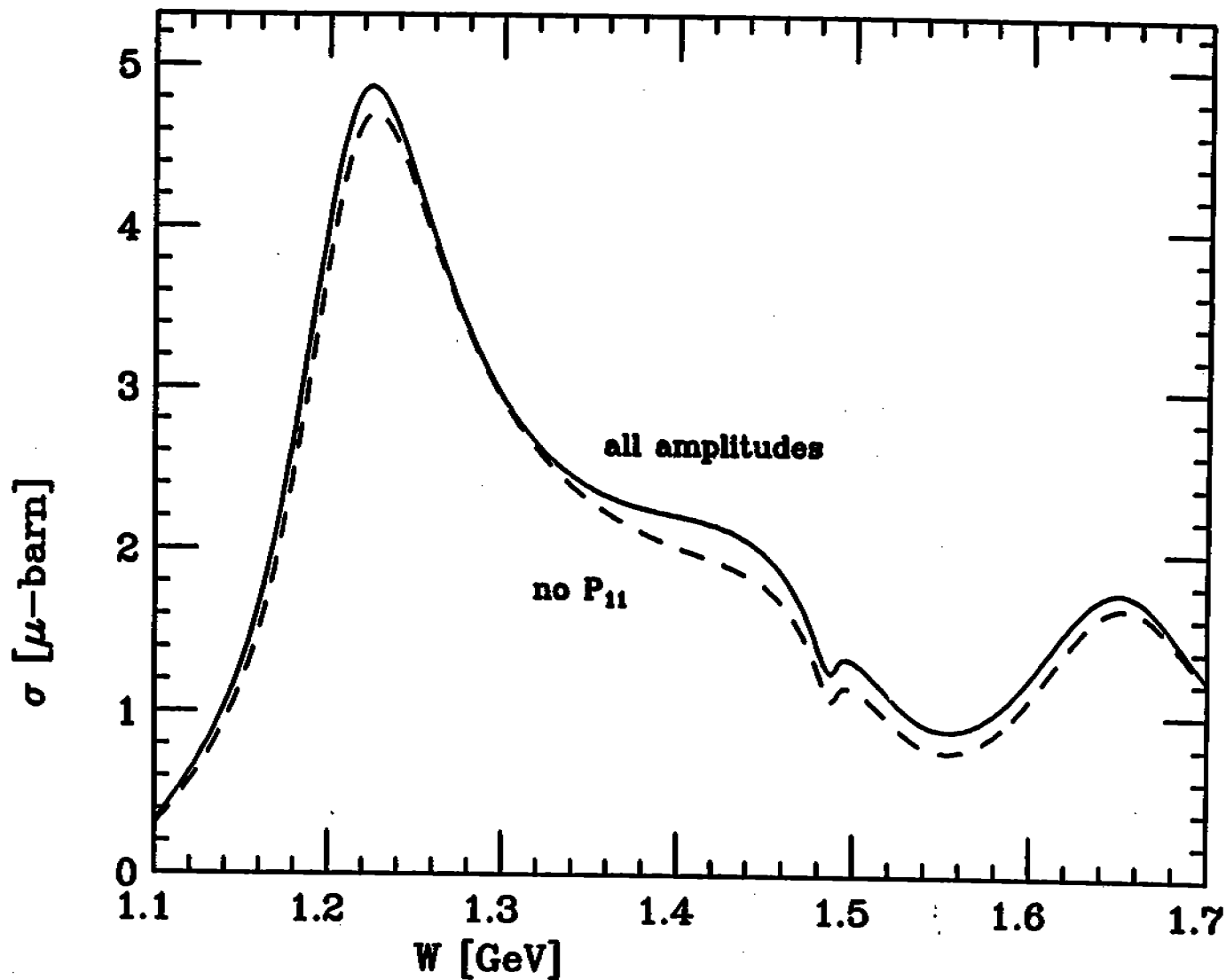
Figure 22 Cross section for p(e,e'p)π^o at the specified kinematics. The amplitudes of the Kroesen analysis[14] were used to compute the cross section with, and without the P_{11} amplitudes.

$\epsilon=0.8$, $\theta^*=0^\circ$, $\phi=90^\circ$

all amplitudes

$S_{11}=0$

$P_{11}=0$
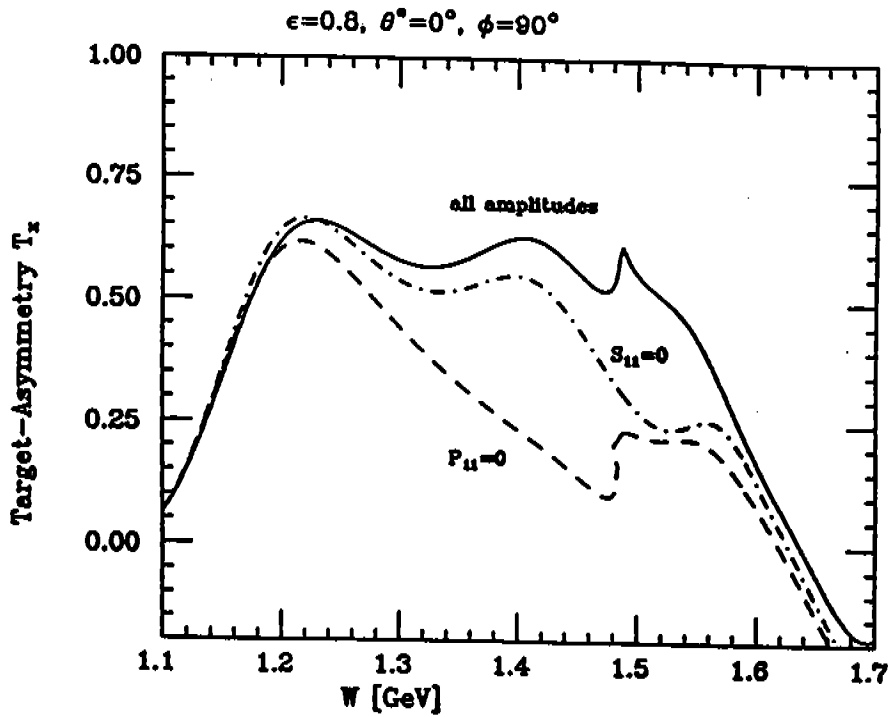
Figure 23 Target asymmetry T_x for p(e,e'p)π° at the specified kinematics. The Kroesen amplitudes [14] were used. The sensitivity to the $P_{11}(1440)$ and $S_{11}(1535)$ is shown.

$W=1.44$GeV, $\epsilon=0.8$, $\phi=90^\circ$

all amplitudes

$P_{11}=0$
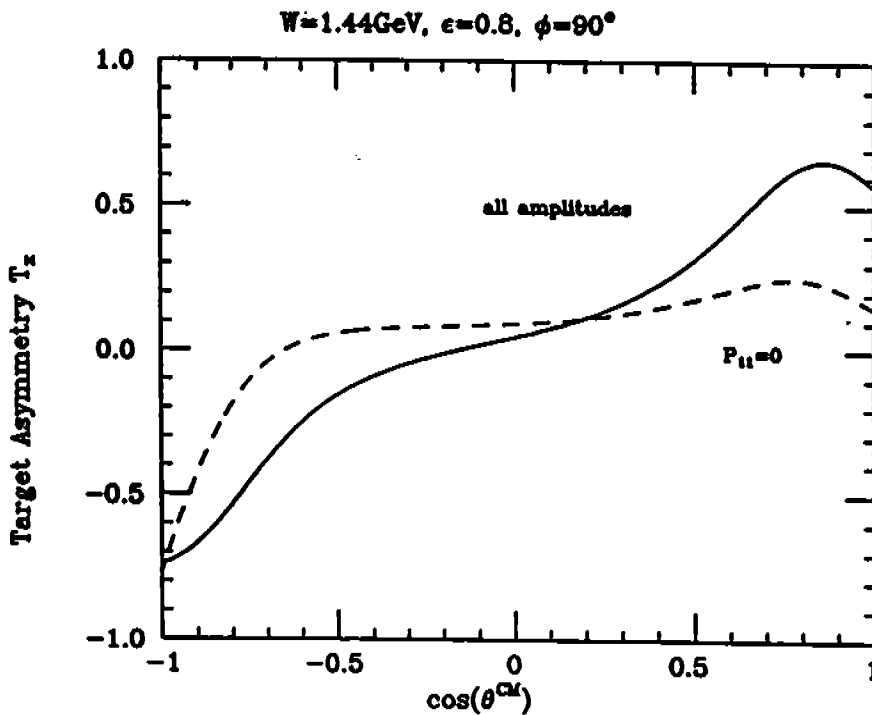
Figure 24 Angular distribution of the polarization asymmetry T_x. Same assumption as in Fig. 23.

Electroproduction: π° at $Q^2 = 1.0$ GeV^2/c^2

$\theta = 135^\circ$, $\phi = 30^\circ$, $\epsilon = 0.8$
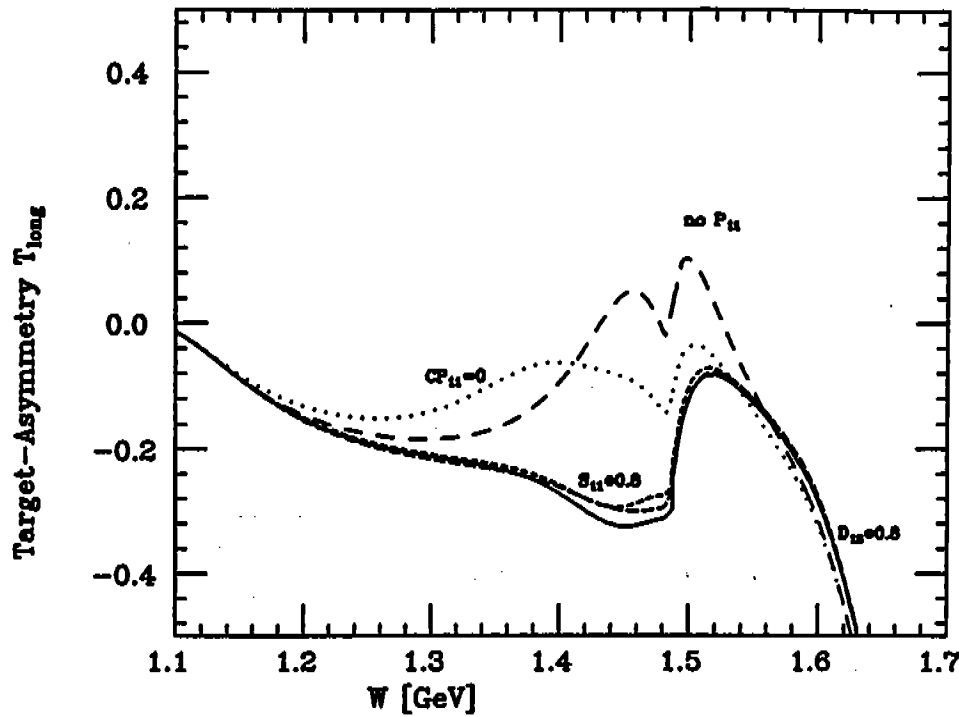
Figure 25 Target asymmetry T_{long} predictions using the Kroesen amplitudes. The sensitivity to various resonant and non-resonant amplitudes is shown (CP_{11} denotes the longitudinal resonant amplitude).
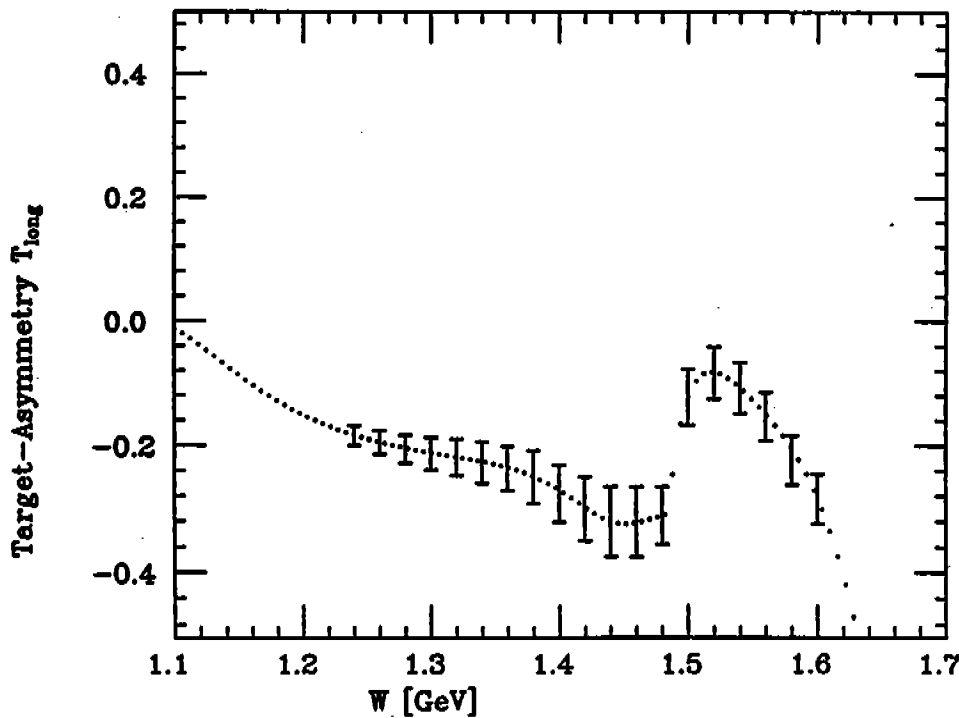
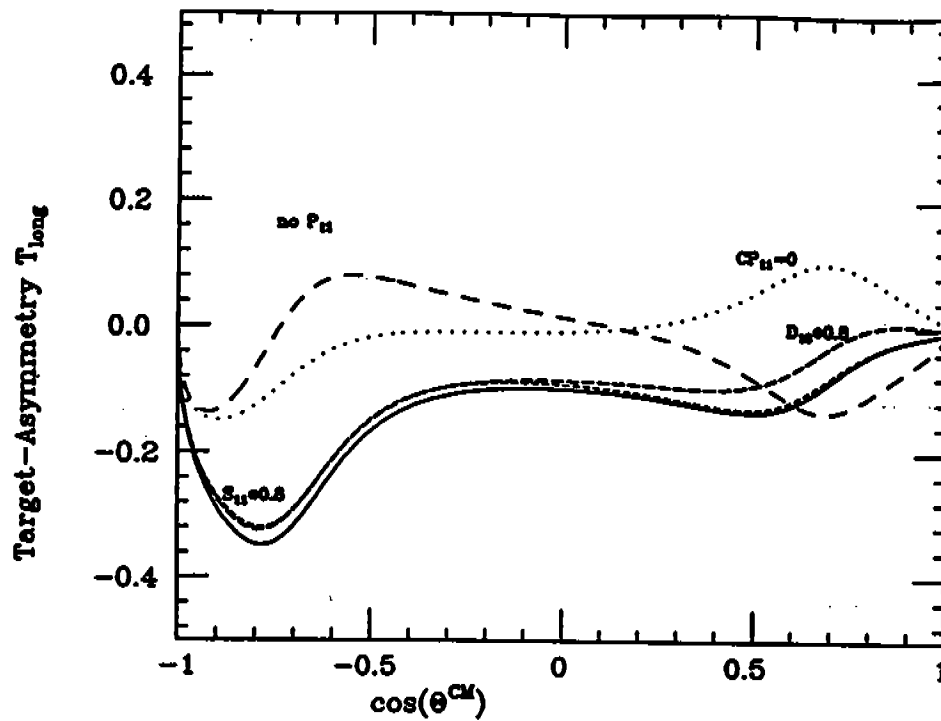**Figure 26** Expected statistical uncertainties for a measurement of T_{long}. The Kroesen amplitudes have been used.

W=1.44GeV, φ=30°, ε=0.8

Figure 27   Same as Figure 25, but different kinematics.
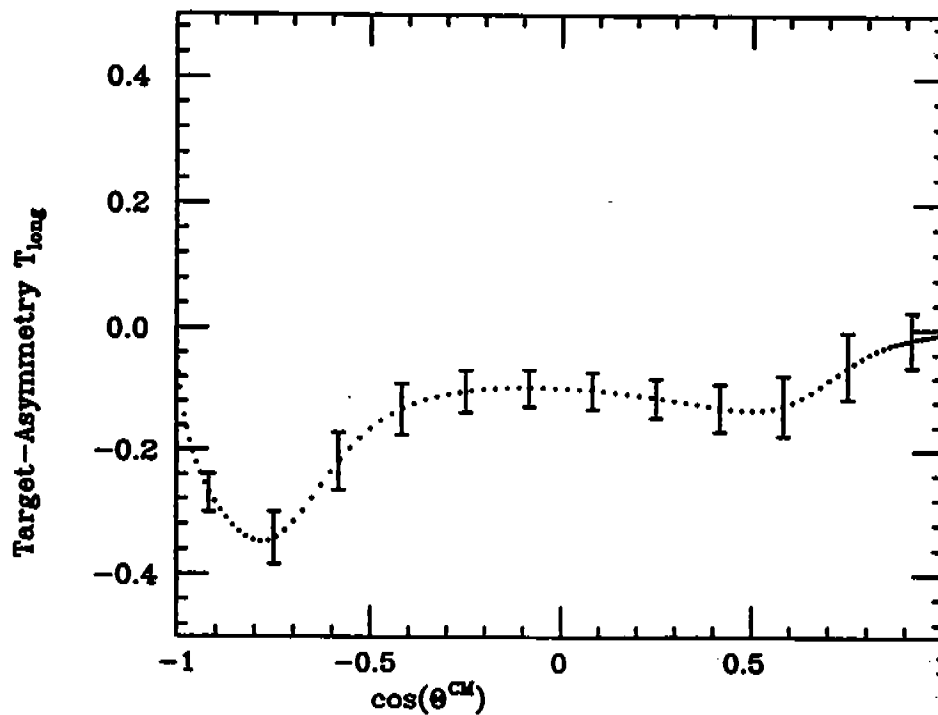
Figure 28   Same as Figure 26, but different kinematics.

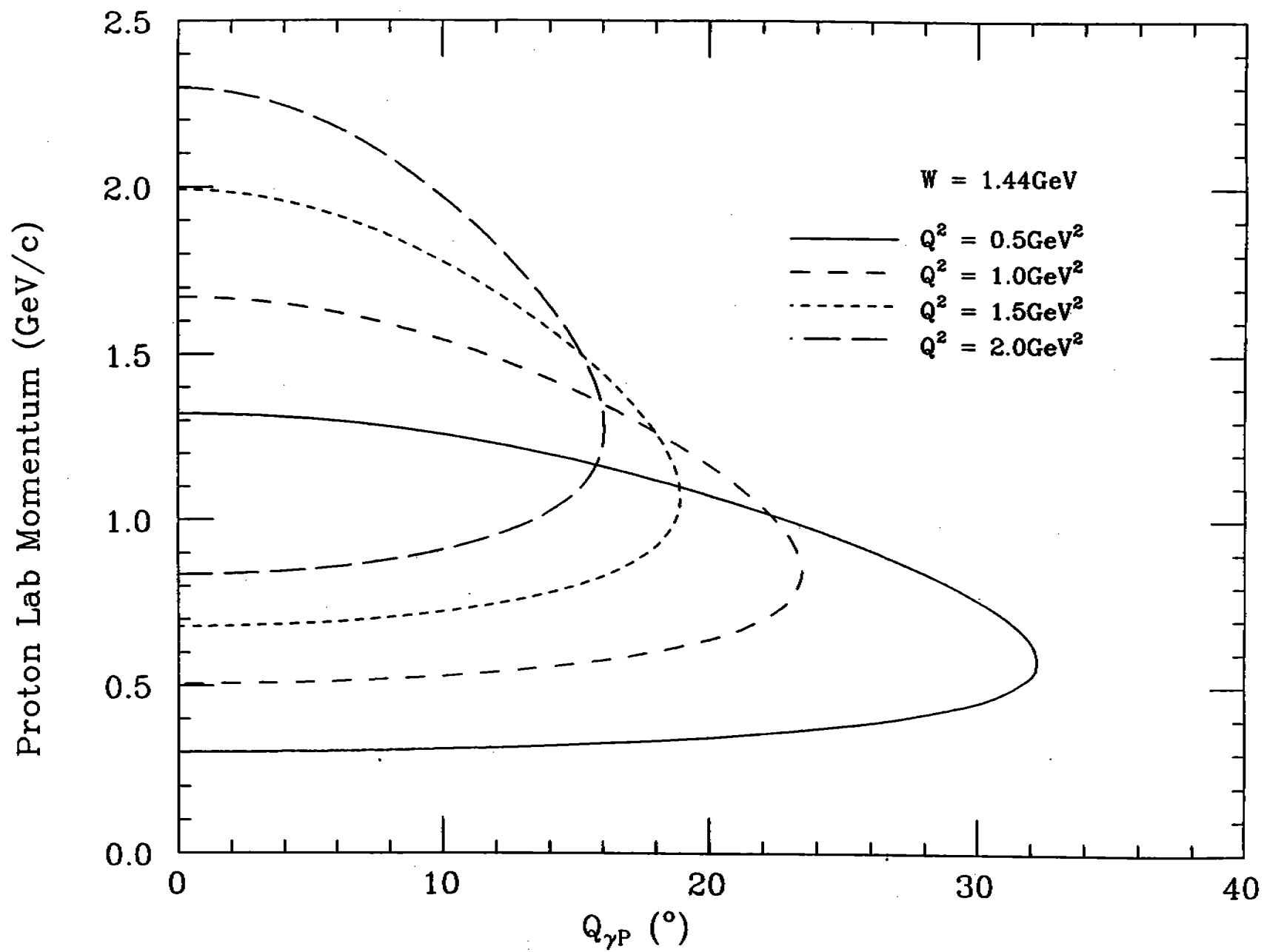**Figure 29** Proton kinematics for p(e,e'p)π^o.
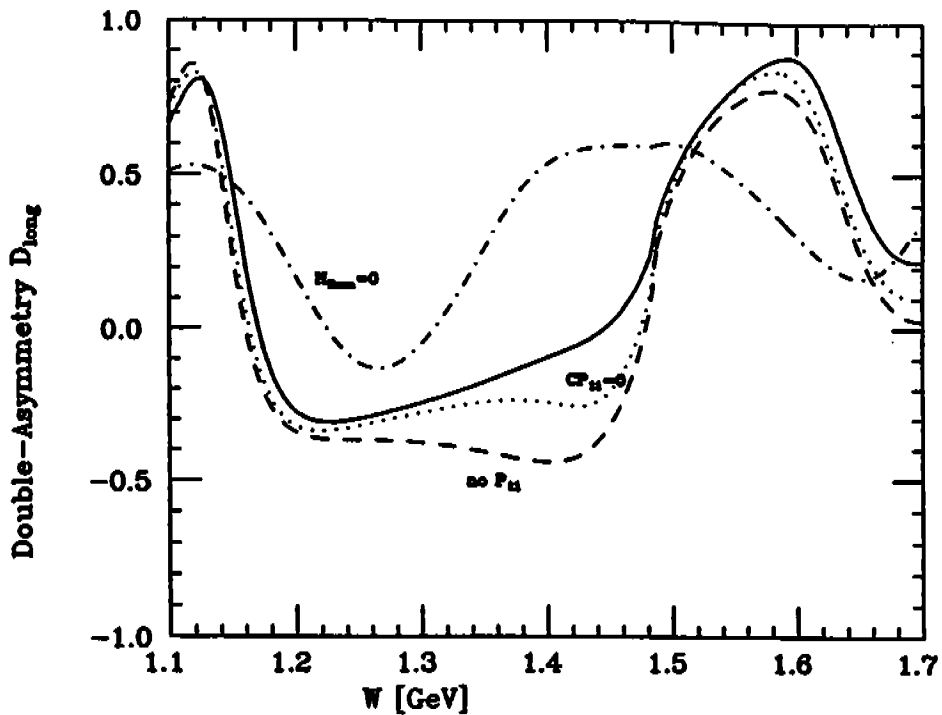
$\theta=115°$, $\phi=180°$, $\epsilon=0.8$

Figure 30 Predicted double polarization asymmetry D_{long} versus W at $\theta° = 115°$, $\phi = 180°$, $\epsilon = 0.8$. The sensitivity to the Born amplitudes, and to the resonant P_{11} amplitudes is shown. The Kroesen amplitudes have been used.
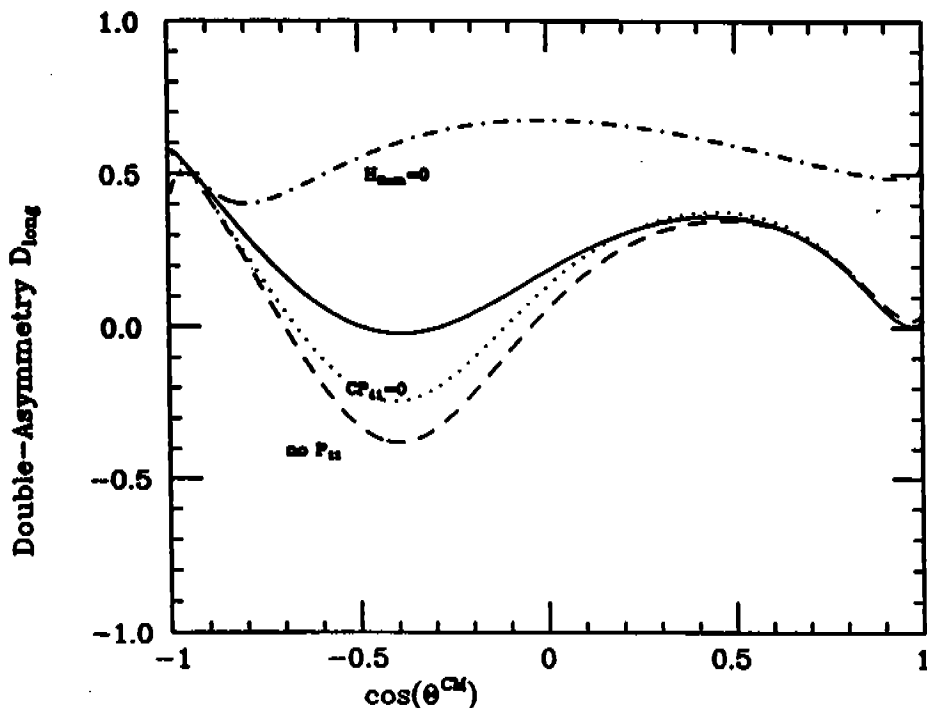
W=1.44GeV, $\phi=180°$, $\epsilon=0.8$

Figure 31 Same as in Figure 30, but different kinematics.